

Highlights

Separation control applied to the turbulent flow around a NACA4412 wing section

Yuning Wang, Fermin Mallor, Carlos Guardiola, Raffaello Mariani, Ricardo Vinuesa

- High-fidelity simulations of a separated wing section with a wide spanwise width.
- Steady and oscillatory uniform blowing/suction control strategies are analyzed.
- A wide range of control parameters are evaluated for separation control.
- Combining steady uniform blowing and suction achieves optimal performance.
- Flow separation is eliminated, with a lift increase of up to 11%.
- Blowing and suction show evident impacts on turbulent boundary layers over the wing.

Separation control applied to the turbulent flow around a NACA4412 wing section

Yuning Wang^a, Fermin Mallor^{a,b}, Carlos Guardiola^c, Raffaello Mariani^a, Ricardo Vinuesa^a

^a*Department of Engineering Mechanics, KTH Royal Institute of Technology, SE-100 44, Stockholm, Sweden*

^b*PredictiveIQ, FL 33067, Parkland, USA*

^c*Departamento de Máquinas y Motores Térmicos, Universitat Politècnica de València, Camino de Vera, s.n., 46022 Valencia, Spain*

Abstract

We carried out high-resolution large-eddy simulations (LESs) to investigate the effects of several separation-control approaches on a NACA4412 wing section with spanwise width of $L_z = 0.6$ at an angle of attack of $AoA = 11^\circ$ at a Reynolds number of $Re_c = 200,000$ based on chord length c and free-stream velocity U_∞ . Two control strategies were considered: (1) steady uniform blowing and/or suction on the suction and/or pressure sides, and (2) periodic control on the suction side. A wide range of control configurations were evaluated in terms of aerodynamic efficiency (i.e., lift-to-drag ratio) and separation delay. Uniform blowing and/or suction effectively delayed flow separation, leading to a lift increase of up to 11%, but yielded only marginal improvements in aerodynamic efficiency. In contrast, periodic control neither enhanced separation delay nor improved efficiency. A detailed analysis of the interaction between uniform blowing and/or suction and turbulent boundary layers (TBLs) over the wing was performed, including assessments of (1) integral boundary-layer quantities, (2) turbulence statistics, and (3) power-spectral densities. Significant modifications in Reynolds stresses and spectral characteristics were observed. To the authors' best knowledge, this is the first numerical study utilizing high-resolution LESs to provide comprehensive assessments on separation control.

Keywords: Flow control, Flow separation, High-fidelity simulations, Turbulent boundary layers, Wings, Adverse pressure gradient

Nomenclature

Latin symbols

b	Spanwise width
c	Chord length
C_d	Drag coefficient
C_l	Lift coefficient
c_f	Skin-friction coefficient
c_p	Pressure coefficient
C_μ	Momentum coefficient
f	Frequency
H_{12}	Shape factor
k	Wave number
L	Length scale
l^*	Viscous length scale
L/D	Lift-to-drag ratio
P	Mean pressure
P_e	Boundary-layer-edge pressure
p	Fluctuating pressure
q	Free-stream dynamic pressure
Re_c	Chord-length-based Reynolds number
Re_τ	Friction Reynolds number
Re_θ	Momentum-thickness-based Reynolds number
t	Flow-over time unit
U_t, V_n, W	Mean component of wall-tangential, wall-normal and spanwise velocity
$\overline{u_t^2}, \overline{v_n^2}, \overline{w^2}$	Fluctuation component of wall-tangential, wall-normal and spanwise velocity
$\overline{u_t v_n}$	Reynolds-shear stress
u	Fluctuating streamwise velocity
U_e	Edge velocity of boundary layer
U_∞	Free-stream velocity
u_τ	Friction velocity
x, y, z	Streamwise, vertical and spanwise distance
x_t, y_n	Wall-tangential and wall-normal distance

Greek symbols

β	Clauser pressure-gradient parameter
δ	Boundary-layer thickness
δ^*	Displacement thickness
δ_{99}	99% boundary-layer thickness
ϵ	Dissipation rate
ℓ_{ctrl}	Streamwise extent of control region
ℓ_{sep}	Streamwise length of flow separation
η	Kolmogorov length scale
Γ	Local force
λ	Wave length
ρ	Density
θ	Momentum thickness
ν	Kinematic viscosity
ψ	Control intensity
τ_w	Wall-shear stress

Abbreviations

AFC	Active flow control
AMR	Adaptive mesh refinement
APG	Adverse pressure gradient
BDF	Backward differentiation formula
DNS	Direct numerical simulation
DRL	Deep reinforcement learning
FFT	Fast Fourier transform
FPG	Favorable pressure gradient
GL	Gauss–Legendre
GLL	Gauss–Lobatto–Legendre
LE	Leading edge
LES	Large-eddy simulation
PS	Pressure side
PSD	Power-spectral density
RANS	Reynolds-averaged Navier–Stokes
SEM	Spectral-element method
SGS	Subgrid scale
SS	Suction side
TBL	Turbulent boundary layer
TE	Trailing edge
U.B	Uniform blowing
U.S	Uniform suction

Subscripts/Superscripts/Operators

$_{ctrl}$	Controlled flow
$_{\infty}$	Free-stream quantity
$_d$	Drag
$_n$	Wall-normal direction
$_f$	Friction
$_l$	Lift
$_p$	Pressure
$_t$	Wall-tangential direction
$_w$	Wall quantity
$_{x\ y\ z}$	Streamwise, vertical and spanwise direction
$\overline{(\cdot)}$	Time-averaged quantity
$+$	Inner-scaled quantity

1. Introductions

Flow separation refers to the detachment of a fluid from a solid surface (Maskell, 1955), which occurs due to a severe adverse pressure gradient (APG) (Simpson, 1989). This phenomenon leads to a significant reduction in near-wall momentum and flow velocity, often resulting in decreased aerodynamic efficiency (Abdolahipour, 2024). In aviation, flow separation is particularly critical during take-off, where low-speed conditions require maximizing lift by increasing the angle of attack (AoA) of the wing. However, as the AoA increases, the APG intensifies, often triggering flow separation before the maximum lift is achieved. This disrupts lift generation and degrades aerodynamic performance. Consequently, separation control is essential for optimizing aerodynamic efficiency, improving emission control, and enhancing economic viability (Fukagata et al., 2024).

The key to delaying flow separation lies in augmenting near-wall momentum (Greenblatt and Wygnanski, 2000). Over the past decades, researchers have explored various separation control strategies. These methods fall into two main categories: passive and active flow control (AFC), based on whether they require an external energy input (Gad-el Hak, 1996). Passive control techniques do not require external energy but instead redistribute momentum to influence flow behavior. A common example is the vortex generator, which creates streamwise vortices that energize the boundary layer, enabling it to resist APGs (Lin, 2002). While effective in delaying flow separation (Neves and Mariani, 2024), vortex generators can increase drag in scenarios where separation is absent (Amitay et al., 2001).

In contrast, AFC methods utilize external energy sources to modify momentum exchange. Compared to passive methods, AFC offers greater efficiency and adaptability since it can be activated or deactivated as needed (Brunton and Noack, 2015). A variety of active control strategies have been investigated, including vibrating flaps (Nishri and Wygnanski, 1998) and acoustic excitation (Huang et al., 1987). Recently, deep reinforcement learning (DRL) has emerged as an innovative AFC technique, demonstrating promising results in separation control (Suárez et al., 2024a,b; Font et al., 2024). DRL leverages the capability of neural networks to model complex nonlinear interactions (Vinuesa et al., 2022).

Among AFC techniques, steady uniform suction and blowing have been widely utilized, with a long history of application (Prandtl, 1904). Steady suction removes low-momentum fluid from the boundary layer while deflecting high-momentum fluid toward the wall, effectively stabilizing the boundary layer (Schlichting and Gersten, 2016). This technique is typically employed on the suction side of airfoils to mitigate separation. Numerous experimental and numerical studies confirm its effectiveness. For instance, Hunter and Johnson (1954) used leading-edge suction on a thin airfoil, successfully eliminating separation. Similar enhancements in maximum lift coefficients have been demonstrated for gliders (Cornish, 1953) and motor planes (Raspert, 1956). Parametric studies (Goodarzi et al., 2012) and large-eddy simulations (LES) (Zhi-yong et al., 2018) further explored suction control performance on various airfoil shapes. Steady uniform blowing increases near-wall momentum by enhancing wall-normal convection. While primarily employed for circulation control (Chen et al., 2012), steady blowing has also been used for drag reduction (Vinuesa and Schlatter, 2017). Combinations of blowing and suction have also been extensively studied. For example, simulations of NACA0012 airfoils (Yousefi and Saleh, 2015) demonstrated improvements in aerodynamic efficiency and separation delay through optimized control configurations.

Beyond steady control methods, periodic-control techniques use oscillatory blowing or suction to introduce additional momentum at specific frequencies, modifying mixing-layer development and delaying separation (Greenblatt and Wygnanski, 2000). Experimental studies on NACA0015 airfoils (Seifert et al., 1996) showed that oscillatory blowing outperformed steady blowing in enhancing maximum lift. Wind-tunnel tests (Tang et al., 2014) and numerical investigations (Abdolahipour, 2023) further highlight the effectiveness of periodic control.

Despite these advancements, several limitations remain. Experimental studies primarily focus on aerodynamic performance metrics (e.g., lift and drag) but lack high-fidelity flow measurements. Moreover, most numerical studies employ Reynolds-averaged Navier–Stokes (RANS) models with two-dimensional domains, potentially overestimating control effectiveness by neglecting three-dimensional effects. To address these gaps, the present study conducts high-resolution LES of a NACA4412 wing section at $AoA = 11^\circ$ and $Re_c = 200,000$ to evaluate steady and oscillatory blowing/suction configurations. This study focuses on a single airfoil type and angle of attack to facilitate direct comparisons with existing studies (Atzori et al., 2020; Mallor et al., 2024a) while maintaining computational feasibility. For higher angles of attack and Reynolds numbers, we refer to the comprehensive database documented in Mallor et al. (2024b). To the best of the authors’ knowledge, this is the first numerical study employing high-resolution LES to provide comprehensive assessments of separation control.

The paper is organized as follows. In § 2, we introduce the numerical setup and control configurations. In § 3, we present findings on (1) control impacts on aerodynamic characteristics, (2) streamwise development of the boundary layer, (3) inner- and outer-scaled wall-normal profiles of turbulence statistics, and (4) spectral analysis. Finally, in § 4, we summarize the results and provide further discussion.

2. Methodology

2.1. High-resolution large-eddy simulation (LES)

We perform high-resolution LES of flow around a NACA4412 wing section at an angle of attack (AoA) of 11° and a Reynolds number of $Re_c = 200,000$ using the incompressible Navier–Stokes solver Nek5000 (Fischer et al., 2008). The solver employs the spectral-element method (SEM) (Patera, 1984), which combines high accuracy with computational efficiency.

The computational domain consists of hexahedral elements, where velocity and pressure are represented using Lagrange interpolants of polynomial order $N = 7$. Following the $\mathbb{P}_N\mathbb{P}_{N-2}$ formulation (Maday and Patera, 1989), velocity is evaluated at N^3 points based on the Gauss–Lobatto–Legendre (GLL) quadrature rule, while pressure is defined on a staggered grid of $(N - 2)^3$ points using the Gauss–Legendre (GL) quadrature. Time integration is performed using an explicit third-order extrapolation (EXT3) scheme for nonlinear terms and an implicit third-order backward differentiation formula (BDF3) for viscous terms. To minimize aliasing errors, overintegration is applied by oversampling nonlinear terms by a factor of $3/2$ in each direction.

An implicit subgrid-scale (SGS) model, based on a time-dependent relaxation-term filter (Negi et al., 2018), accounts for the dissipation of unresolved scales, which is able to resolve $\approx 90\%$ of the total dissipation (Eitel-Amor et al., 2014). This model operates through a volume force applied to a subset of spectral-element modes and has been validated in wing simulations by Vinuesa et al. (2018). We refer to Negi et al. (2018) for the details of implementation. Boundary-layer tripping is implemented via volume forcing (Hosseini et al., 2016), applied at the streamwise location $x/c = 0.1$ on both suction and pressure sides. The tripping parameters follow Hosseini et al. (2016) and are adjusted to the present setup using local laminar boundary-layer scales (i.e., the edge velocity U_e and boundary-layer thickness δ^*). This formulation ensures consistency across different computing environments and compilers (Mallor et al., 2024b). Further details on the Nek5000 implementation are provided by Massaro et al. (2024). Note that the tripping force, imposed at $x/c = 0.1$, ensures flow reattachment shortly downstream of the leading edge. As a result, the presence of a leading-edge separation bubble does not affect the flow development further downstream.

The computational domain (see fig. 1) is a rectangular box with streamwise and vertical dimensions of $L_x = 50$ and $L_y = 40c$ (Vinuesa et al., 2015) with a spanwise length of $L_z = 0.6c$. The leading (LE) and trailing edges (TE) of the airfoil are positioned at $-0.5c$ and $0.5c$ from the domain center, respectively. The airfoil is rotated to achieve $AoA = 11^\circ$. Boundary conditions are defined as follows: the front, upper, and lower boundaries use Dirichlet conditions, with a constant inflow velocity U_∞ applied at the left boundary. The top and bottom boundaries enforce a normal outflow condition with tangential velocity U_∞ . For the right (outflow) boundary, a modified Neumann condition (Dong et al., 2014) is used to prevent uncontrolled influx of kinetic energy.

The simulation employs adaptive mesh refinement (AMR) and non-conformal meshing to optimize accuracy while maintaining computational efficiency. Unlike prior studies that relied on conformal meshes (Hosseini et al., 2016; Vinuesa et al., 2018), which often led to excessive resolution and degraded pressure-solver performance, the present setup allows for a larger spanwise extent of $L_z = 0.6c$. This spanwise width is sufficient to capture the dominant turbulent structures in the boundary layer (Vinuesa et al., 2018).

The choice of L_z is motivated by the need to resolve separation physics, as smaller domains can artificially constrain separation dynamics. Mallor et al. (2024b) suggest that a spanwise width of at least $0.4c$ is needed to prevent artificial domain-induced constraints on turbulence dynamics. The present setup satisfies this criterion and exceeds the spanwise extent used in previous high-fidelity wing simulations at high angles of attack (Sato et al., 2017; Asada and Kawai, 2018; Tamaki and Kawai, 2023). These choices are further supported by recent experimental findings (Mallor et al., 2025).

The h -type AMR strategy in Nek5000 (Offermans, 2019) ensures that the mesh resolution adheres to high-resolution LES standards, closely approaching direct numerical simulation (DNS) accuracy (Negi et al., 2018). The computational domain consists of approximately 3.9×10^8

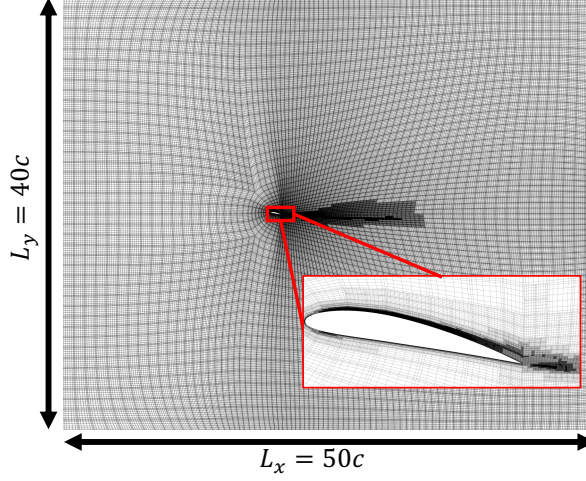


Figure 1: Two-dimensional plane of the spectral-element mesh used in the computational domain. The inset illustrates the mesh refinement near the airfoil surface. The domain is three-dimensional with a spanwise width of $L_z = 0.6c$, containing approximately 3.9×10^8 grid points after applying adaptive mesh refinement (AMR).

grid points after AMR is applied to the non-conformal mesh. Near-wall spatial resolutions are defined in viscous units as follows: $\Delta x_t^+ < 18.0$, $\Delta y_n^+ < (0.64, 11.0)$, and $\Delta z^+ < 9.0$ in the tangential, normal, and spanwise directions, respectively. The viscous length scale is defined as $l^* = \nu/u_\tau$, where $u_\tau = \sqrt{\tau_w/\rho}$ is the friction velocity, and $\tau_w = \rho\nu(dU_t/dy_n)_{y_n=0}$ is the mean wall-shear stress. In the wake, to ensure the streamwise resolution is fine enough to resolve the convecting structures (Spalart, 1997), the spatial resolution is designed to satisfy $\Delta x/\eta < 9$, where $\eta = (\nu^3/\epsilon)^{1/4}$ is the Kolmogorov length scale and ϵ is the local isotropic dissipation rate.

The AMR process follows these steps: first, isotropic elements are clustered in an oct-tree structure using the *p4est* library (Burstedde et al., 2011), with interpolation operators (Kruse, 1997) ensuring continuity at non-conformal interfaces. An *a-posteriori* spectral error indicator (Mavriplis, 1990) identifies elements requiring refinement by measuring truncation and quadrature errors. Refinement is applied iteratively until convergence is reached and the mesh meets the resolution criteria. Note that the refinement is homogeneous in the spanwise direction. For details on AMR implementation in Nek5000 and validation against conformal wing simulations, see Tanarro et al. (2020).

2.2. Control Configurations

Tab. 1 summarizes the control configurations considered in this study, which employ steady uniform blowing and suction to delay flow separation. Note that we explored periodic control over the suction side and other configurations of uniform suction (see Appendix A) to enhance reattachment and aerodynamic efficiency. However, the periodic configurations generally did not outperform the cases listed in tab. 1 in terms of separation delay or aerodynamic efficiency. Thus, the analysis focuses on Cases A–E.

The primary configuration combines uniform suction (U.S.) on the suction side (SS) with uniform blowing (U.B.) on the pressure side (PS). The control intensity ψ varies as $\psi = 0.25\%U_\infty$, $0.50\%U_\infty$, and $1.0\%U_\infty$ corresponding to Case A, Case B, and Case C, respectively. Case A

replicates the optimized configuration from [Mallor et al. \(2024a\)](#), which was obtained using Bayesian optimization in a 2D RANS simulation of the NACA4412 airfoil at $AoA = 11^\circ$ and a higher Reynolds number ($Re_c = 1,000,000$). This setup demonstrated significant improvements in aerodynamic efficiency and separation delay. However, due to RANS limitations, the control intensity was restricted to $\psi = 0.25\%U_\infty$ to prevent non-physical solutions. The high-resolution LES in the present study allows for higher control intensities while maintaining physical consistency. Additionally, configurations with only uniform suction on the suction side (Case D) and only uniform blowing on the pressure side (Case E) are considered to assess the individual effects of each control method. These cases provide insights into the efficiency of different strategies in improving aerodynamic performance and delaying separation.







Case notation	Control method	Control area	Input intensity (ψ)	Color code
Ref	Uncontrolled	—	—	
Case A	U.S. at SS & U.B. at PS	$0.25 \leq x/c \leq 0.86$	$0.25\%U_\infty$	
Case B	U.S. at SS & U.B. at PS	$0.25 \leq x/c \leq 0.86$	$0.50\%U_\infty$	
Case C	U.S. at SS & U.B. at PS	$0.25 \leq x/c \leq 0.86$	$1.00\%U_\infty$	
Case D	U.S. at SS	$0.25 \leq x/c \leq 0.86$	$0.25\%U_\infty$	
Case E	U.B. at PS	$0.25 \leq x/c \leq 0.86$	$0.25\%U_\infty$	

Table 1: Control configurations considered in the present study on a NACA4412 wing section at $AoA = 11^\circ$ and $Re_c = 200,000$. The colored squares denote the color code for each case.

The control region spans from $x/c = 0.25$ to 0.86 (see fig. 2), which aligns with previous studies ([Vinueza and Schlatter, 2017](#); [Atzori et al., 2020, 2021](#); [Wang et al., 2024](#)), enabling a direct comparison of control effects. Blowing and suction are imposed as Dirichlet boundary conditions at the wall, where the horizontal and vertical velocity components are adjusted to ensure that the wall-normal velocity (V_n) matches the prescribed control intensity ([Wang et al., 2024](#)). Note that the boundary conditions for both the wall-tangential and spanwise velocity components are of Dirichlet type, and are set to zero in accordance with the no-slip condition.

For each case, simulations were run for at least 2 flow-over times (i.e., the time required for a fluid particle to traverse a distance of c at velocity U_∞) to ensure statistical convergence. Note that for the controlled cases, the simulations were initialized from a fully-developed turbulent field of the uncontrolled case. [Vinueza et al. \(2016\)](#) suggested that statistical convergence depends on both time averaging and the spanwise width. [Vinueza et al. \(2018\)](#) reported that ≈ 10 flow-over times were required for a wing section with $L_z = 0.1c$ at $Re_c = 200,000$. Due to the larger spanwise width ($L_z = 0.6c$) in our setup, the achieved convergence here is equivalent to ≈ 12 flow-over times for a domain with $L_z = 0.1c$. However, for cases presented in [Appendix A](#), a shorter averaging time of ≈ 1.6 flow-over times was used, which is sufficient for evaluating aerodynamic characteristics. The computational cost for simulating 2 flow-over times is approximately 1.0 million CPU hours on a Cray-XC40 system.

3. Results

In this section, we first evaluate the aerodynamic characteristics of the wing section under various control configurations. Next, we analyze the integral quantities of streamwise boundary-layer development, followed by an assessment of wall-normal profiles of turbulence statistics,

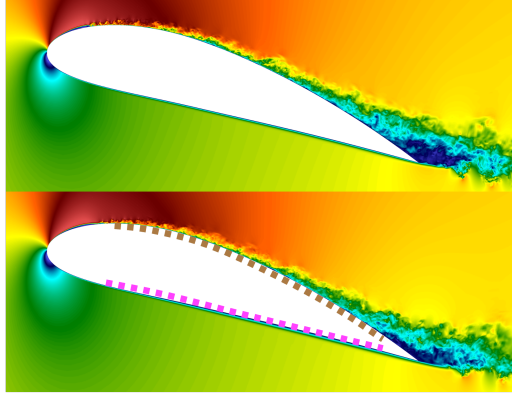


Figure 2: Snapshots of the horizontal velocity component at an arbitrary time step for (top) the uncontrolled case and (bottom) Case A. The velocity values range from $-0.2U_\infty$ (dark blue) to $1.8U_\infty$ (dark red). Differences in boundary-layer thickness on both sides and the extension of attached flow downstream over the suction side are evident. The control regions for uniform suction on the SS. and uniform blowing on the PS. are indicated by dashed brown and magenta lines, respectively.

including mean and fluctuating velocity components. Finally, we examine the time-series data using spectral analysis in terms of space and time.

3.1. Aerodynamic characteristics

We begin by assessing the control effect on aerodynamic characteristics, specifically focusing on separation delay and aerodynamic efficiency. The separation delay is quantified by the streamwise length of the separated flow (ℓ_{sep}), defined as:

$$\ell_{\text{sep}} = (x_{\text{TE}} - x_{\text{sep}})/c, \quad (1)$$

where x_{TE} is the trailing-edge location, x_{sep} is the separation onset point where the skin-friction coefficient c_f becomes negative, and c is the chord length.

Another key metric for separation control is the momentum coefficient C_μ , which governs the control effect through momentum addition (Poisson-Quinton, 1948), given by:

$$C_\mu = \frac{\rho \psi^2 \ell_{\text{ctrl}}}{\frac{1}{2} \rho U_\infty^2}, \quad (2)$$

where ℓ_{ctrl} is the streamwise extent of the control region. Note that for configurations that combine suction on the suction side and blowing on the pressure side, C_μ is doubled.

The aerodynamic efficiency is evaluated using the lift-to-drag ratio (L/D), where the lift and drag coefficients are defined as:

$$C_l = \frac{f_l}{bq}, \quad C_d = \frac{f_d}{bq}, \quad (3)$$

where b is the spanwise width, f_l/b and f_d/b are the lift and drag forces per unit length, and $q = \frac{1}{2} \rho U_\infty^2$ is the free-stream dynamic pressure. The drag coefficient is further decomposed into skin-friction drag ($C_{d,f}$) and pressure drag ($C_{d,p}$) such that $C_d = C_{d,f} + C_{d,p}$.

Name	ℓ_{sep}	$C_\mu [\times 10^{-5}]$	C_l	$C_{d,p}$	$C_{d,f}$	$C_d = C_{d,p} + C_{d,f}$	L/D
Ref	0.14	0.0	1.314	0.0450	0.0078	0.0527	24.876
Case A	0.02 (−85%)	1.52	1.355 (+3.2%)	0.0473 (+5.3%)	0.0083 (+5.5%)	0.0556 (+5.37%)	24.36 (−2.06%)
Case B	0.00 (−100%)	6.10	1.392 (+5.9%)	0.0488 (+8.55%)	0.0099 (+26.46%)	0.0587 (+11.21%)	23.67 (−4.73%)
Case C	0.00 (−100%)	24.4	1.463 (+11.45%)	0.0519 (+15.53%)	0.0145 (+85.29%)	0.0665 (+25.88%)	22.02 (−11.47%)
Case D	0.02 (−85%)	0.76	1.326 (+0.95%)	0.0466 (+3.57%)	0.0096 (+15.75%)	0.0566 (+5.38%)	23.829 (−4.21%)
Case E	0.05 (−64%)	0.76	1.312 (−0.13%)	0.0457 (+1.10%)	0.0069 (−12.47%)	0.0523 (−0.915%)	25.073 (+0.79%)

Table 2: Separation length (ℓ_{sep}), momentum coefficient (C_μ), lift coefficient (C_l), drag components ($C_{d,p}$ and $C_{d,f}$), total drag (C_d), and aerodynamic efficiency (L/D) for the cases in tab. 1. Percent changes from the reference case are shown in parentheses.

Tab. 2 presents the control impact on aerodynamic performance. The uncontrolled flow separates at $x/c = 0.86$, yielding $\ell_{\text{sep}} = 0.14$, which remains consistent across Reynolds numbers at $AoA = 11^\circ$ (Mallor et al., 2024b). With control, separation is significantly delayed. Case A reduces ℓ_{sep} to 0.02, whereas Cases B and C fully eliminate separation, achieving complete reattachment. This is directly linked to the increasing of C_μ , whose relation with ℓ_{sep} is clearly demonstrated by fig. 3. However, solely applying uniform suction over suction side (Case D) yield the same ℓ_{sep} as combined control (Case A) while the C_μ of Case D is half of that of Case A. Moreover, solely uniform blowing over pressure side (Case E) yields a lower $\ell_{\text{sep}} = 0.05$. The results indicate that suction over the suction side is dominant for delaying flow separation.

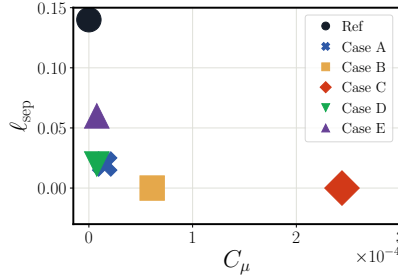


Figure 3: The length of separation region ℓ_{sep} as a function of momentum coefficient C_μ . The color code follows tab. 1.

On the other hand, although the control consistently increases C_l up to 11.45%, aerodynamic efficiency is more sensitive to changes in total drag. Fig. 4(a) shows the decomposition of the total drag into $C_{d,f}$ and $C_{d,p}$. The control primarily increases skin-friction drag, with a smaller increase in pressure drag, which dominates at high angles of attack. As consequence, total drag increases significantly with higher control inputs, particularly in Case C, where both drag components increase drastically. Fig. 4(b) illustrates the relationship between C_l and C_d . The control configurations did not improve aerodynamic efficiency except in Case E. In particular, at $\psi = 1.0\%U_\infty$ (Case C), the control drastically degrades the aerodynamic efficiency, reducing L/D by 11.47% although Case C achieved the highest lift ($C_l = 1.46$), its L/D decreased by 11.5% due to a 25.8% increase in total drag. This highlights the trade-off between lift enhancement and drag penalty at higher control intensities. Note that the L/D values of Case A is in contrast with those reported by Mallor et al. (2024a), where the same control configuration improved L/D by 42%. However, their study was based on 2D RANS simulations at a higher Reynolds number ($Re_c = 1,000,000$), which may overestimate the control performance due to

the absence of spanwise and Reynolds number effects, as well as the effect of the turbulence model.

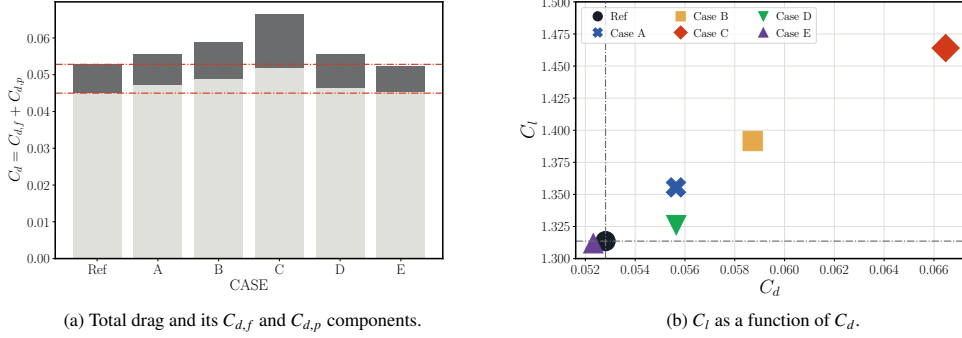


Figure 4: (a) Total drag for all considered cases, where the $C_{d,f}$ and $C_{d,p}$ components are colored in light and dark gray, respectively. Note that the uncontrolled $C_{d,f}$ and $C_{d,p}$ are denoted by red dash-dotted lines. (b) Relation between lift and drag, where the dash-dotted lines indicate the C_l and C_d of the uncontrolled case, respectively.

Moreover, Case D reduces L/D by 4.21%, with minimal lift improvement and a 1.1% increase in $C_{d,p}$, while Case E is the only case that yields a marginal improvement in L/D by reducing $C_{d,f}$ while minimally increasing $C_{d,p}$. These findings are distinct from those at $AoA = 5^\circ$ and the same Reynolds number. Using $\psi = 0.2\%$ with same control area, uniform suction over the suction side improved L/D by significantly increasing C_l and reducing $C_{d,p}$, albeit with a slight increase in $C_{d,f}$, whereas uniform blowing over the pressure side improved L/D by reducing both $C_{d,p}$ and $C_{d,f}$ outlined by [Atzori et al. \(2020\)](#). These results suggest that control strategies effective for attached flows may not be suitable for separation control, as flow properties differ significantly at high angles of attack.

Furthermore, we assess the distribution of lift and drag forces around the wing section. The integrated lift and drag forces can be expressed as:

$$\begin{aligned} f_l &= \int_{\Xi} \Gamma_l d\xi, \\ f_d &= \int_{\Xi} \Gamma_d d\xi, \end{aligned} \quad (4)$$

where Γ_l and Γ_d are the local lift and drag forces, respectively, and Ξ is the perimeter of the airfoil with ξ as the curvilinear coordinate along it ([Atzori et al., 2020](#)). The local forces can be further decomposed into contributions from friction and pressure forces as follows:

$$\begin{aligned} \Gamma_l &= \Gamma_{l,f} + \Gamma_{l,p}, \\ \Gamma_d &= \Gamma_{d,f} + \Gamma_{d,p}, \end{aligned} \quad (5)$$

where the subscripts f and p refer to friction and pressure force components, respectively. Fig. 5 (a) and (b) show the distributions of local lift and drag forces, along with the respective contributions of friction and pressure.

As shown in fig. 5(a), the pressure component $\Gamma_{l,p}$ dominates the lift generation, while the friction component $\Gamma_{l,f}$ is negligible, on the order of $\sim O(-6)$. Regarding drag (fig. 5(b)), the

pressure component $\Gamma_{d,p}$ is also dominant, with $\Gamma_{d,f}$ smaller by an order of magnitude—consistent with the relationship between $C_{d,p}$ and $C_{d,f}$.

Notably, as the only case that improves aerodynamic efficiency, **Case D** shows a clear reduction in Γ_d , particularly by decreasing $\Gamma_{d,p}$ in the region $x/c = 0.1$ to 0.3 . This behavior is not observed in the profiles of the other control cases.

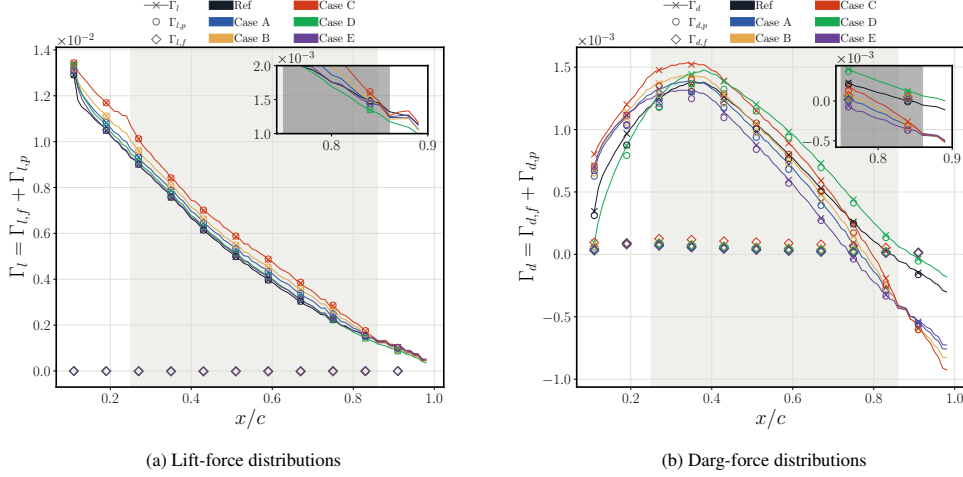


Figure 5: (a) Lift (Γ_l) and (b) drag (Γ_d) force and its friction-force and pressure-force components around the airfoil as a function of x/c . The solid line with cross marker denotes the local force while the cricle and dimonand markers denote its pressure- and friction-force components, respectively. Note that the control region is indicated in light and deep gray for panels and inspections, respectively. The color code follows tab. 1.

3.2. Streamwise development of the boundary layer

The distinct modifications in friction and pressure drag achieved by different control configurations motivate an investigation into the interactions between control and turbulent boundary layers (TBLs) over the wing surfaces. In this section, we assess the effects of control on integral quantities of TBLs. The 99% boundary-layer thickness (δ_{99}) and the mean velocity at the boundary-layer edge (U_e) are determined using the method proposed by [Vinuesa et al. \(2016\)](#).

Fig. 6(a) depicts the streamwise evolution of the skin-friction coefficient ($c_f = \tau_w / (\frac{1}{2}\rho U_e^2)$, where τ_w is the wall-shear stress) on the suction and pressure sides of the airfoil. The impact of control on separation delay is evident. Uniform suction on the suction side increases c_f by enhancing near-wall momentum, with effects proportional to the input intensity (ψ). On the contrary, uniform blowing reduces c_f on the pressure side by removing high-momentum flow away from the wall. These observations align with the findings of [Kametani et al. \(2015\)](#).

Additionally, control influences flow regions upstream of the control area. On the suction side, a significant reduction in c_f occurs upstream of the control region, proportional to ψ . This effect was not observed at $AoA = 5^\circ$ ([Atzori et al., 2020](#)), suggesting distinct interactions between control and stronger adverse pressure gradients (APGs) in separated flows. Notably, individual applications of suction or blowing yield similar effects on c_f as their combined use.

Fig. 6(b) shows the pressure coefficient ($c_p = (P_w - P_0) / (\frac{1}{2}\rho U_\infty^2)$, where P_w and P_0 are the mean wall pressure and static pressure, respectively) on the suction and pressure sides. Control enhances c_p on the pressure side, increasing its value from the stagnation point ($c_p = 1$) to the

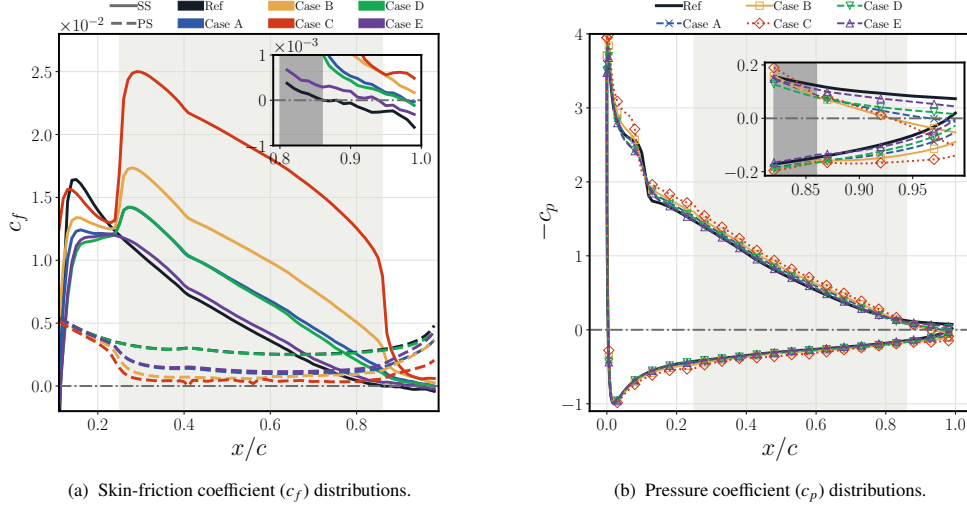


Figure 6: (a) Skin-friction coefficient (c_f) distributions on the suction and pressure side of NACA4412 at $AoA = 11^\circ$ and $Re_c = 200,000$, where the solid and dashed lines denote the distributions on the suction and pressure side, respectively. The gray dash-dotted line denotes the position where $c_f = 0$. (b) Pressure coefficient (c_p) distributions on the suction and pressure side. Note that the control region is indicated in light and deep gray for panels and inspections, respectively. The color code follows tab. 1.

TE. On the suction side, c_p exhibits a downward shift upstream of the control region, followed by an upward shift downstream, mimicking the effects of increased AoA (Mallor et al., 2024a). Note that the Reynolds-number and pressure-gradient effects are disentangled for this wing profile (Pinkerton, 1937), suggesting that the control effects on c_p are consistent across different Reynolds numbers.

Next, we further assess integral quantities of TBLs including the Clauser pressure-gradient parameter $\beta = \delta^* / \tau_w dP_e / dx_t$ (where δ^* is the displacement thickness and P_e is the pressure at the boundary-layer edge), the momentum-thickness-based Reynolds number $Re_\theta = U_e \theta / \nu$ (where θ is the momentum thickness), the friction Reynolds number $Re_\tau = \delta_{99} u_\tau / \nu$ and the shape factor $H_{12} = \delta^* / \theta$. Fig. 7 shows their streamwise distributions on both suction and pressure side of the wing profiles. Additionally, the profiles of local edge velocity (U_e) (fig. 7(e)) and 99% boundary-layer thickness (δ_{99}) (fig. 7(f)) are provided for the sake of future reference, as these quantities are particularly sensitive to boundary-layer development and control effects.

At $AoA = 11^\circ$, β ranges from -0.1 to 300 , indicating highly non-equilibrium TBLs (fig. 7(a)). The uncontrolled case exhibits rapid increases on the suction side and gradual decreases on the pressure side, indicating the strong adverse-pressure-gradient (APG) and favorable-pressure-gradient (FPG) conditions, respectively. Uniform suction over the suction side significantly attenuates β . In particular, the profiles of Case C exhibit a nearly constant $\beta \approx 0.64$ until $x/c = 0.8$, followed by a sharp increase, which indicates effective TBL stabilization. Uniform blowing on the pressure side increases $|\beta|$, intensifying the FPG conditions. Moreover, note that Cases B and C exhibit downstream effects on β , while the profiles of Case A and the reference case collapse downstream.

Fig. 7(b) shows the streamwise evolution of Re_θ . The uncontrolled case exhibits rapid growth on both sides, indicating strong boundary-layer development. Uniform suction over the suction

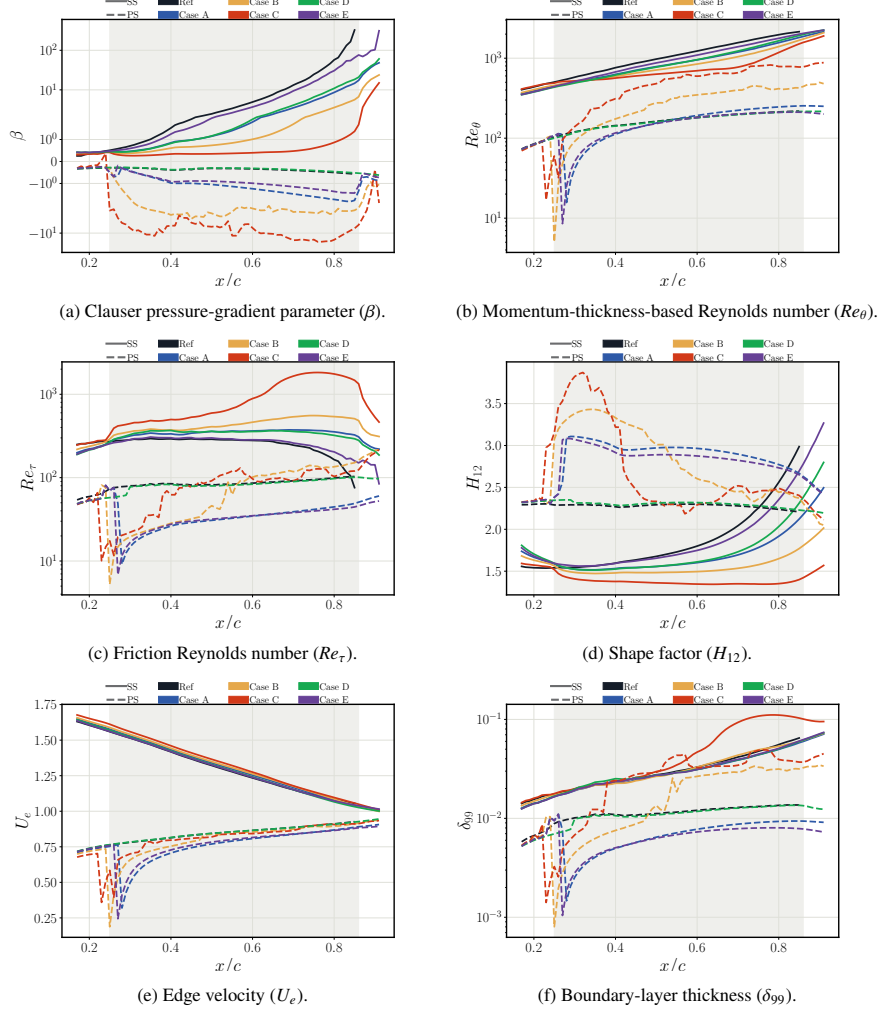


Figure 7: (a) Clauser pressure-gradient parameter (β), (b) momentum-thickness-based Reynolds number (Re_θ), (c) friction Reynolds number (Re_τ), (d) shape factor (H_{12}), (e) Edge velocity (U_e) and (f) boundary-layer thickness (δ_{99}) as a function of streamwise location x/c on the suction side (solid lines) and pressure side (dashed lines) of NACA4412 at $AoA = 11^\circ$ and $Re_c = 200,000$. Note that the control region is indicated in gray. The color code follows tab. 1.

side decelerates Re_θ growth by deflecting high-momentum flow toward the wall (Kametani et al., 2015; Atzori et al., 2021), while uniform blowing on the pressure side accelerates Re_θ growth by thickening the boundary layer. Note that the spikes at the beginning of control area is due to the modification of the boundary-condition type.

Fig. 7(c) depicts the distributions of Re_τ , directly linked to the variation of friction velocity (u_τ). The uncontrolled case shows a rapid decrease of Re_τ on the suction side due to the intensified APGs downstream. Uniform suction mitigates this decline by increasing u_τ , proportional to ψ , which is also demonstrated in fig. 6 (a). The effect of blowing over the pressure side depends on the input intensity: for Cases B and C, profiles start deviating above the uncontrolled case

at $x/c = 0.45$ and 0.56 , respectively, due to increased δ_{99} and APG effects (Harun et al., 2013; Pozuelo et al., 2022). In contrast, Case A consistently suppresses Re_τ within the control area.

Fig. 7(d) depicts the streamwise development of shape factor H_{12} . Higher H_{12} values indicate more laminar-like flow, with $H_{12} \geq 2$ characteristic of a Blasius boundary layer. Suction significantly reduces H_{12} , preventing re-laminarization by adding near-wall momentum, whereas blowing increases H_{12} , promoting re-laminarization.

Note that the profiles of Cases D and E closely match those of the reference case and Case A, respectively, indicating that suction over the suction side has minimal influence on the pressure side and vice versa. This observation aligns with the conclusions from Atzori et al. (2020); Fahland et al. (2023).

3.3. Wall-normal profiles of turbulence statistics

The analysis of integral quantities has highlighted the interactions between control and TBLs in terms of streamwise development. In this section, we examine the inner- and outer-scaled profiles of turbulence statistics, focusing on mean velocity components and Reynolds stresses.

The assessment is conducted at $x/c = 0.75$, within the control area. This location is chosen for two reasons: (1) pressure-gradient effects are highly pronounced at this location, and (2) many previous studies (Vinuesa et al., 2018; Atzori et al., 2021; Fahland et al., 2023; Mallor et al., 2024b; Wang et al., 2024) have documented profiles at this location, facilitating future comparisons. Tab. 3 summarizes the integral quantities obtained at $x/c = 0.75$ for all cases. The aforementioned control effects of boundary-layer developments are clearly quantified, leading to significant modifications in turbulence statistics.

Side	Case	u_τ	U_e	δ_{99}	c_f	c_p	β	Re_θ	Re_τ	H_{12}
SS	Ref	0.021	1.11	0.059	0.0009	-0.23	27.97	1802.0	206.9	2.31
	Case A	0.041	1.11	0.045	0.0033	-0.26	5.85	1395.3	366.9	1.80
	Case B	0.056	1.12	0.050	0.0061	-0.28	2.58	1230.9	554.5	1.58
	Case C	0.083	1.13	0.120	0.0139	-0.32	0.64	964.8	1825.5	1.35
	Case D	0.038	1.10	0.055	0.0029	-0.23	7.21	1462.3	340.4	1.88
	Case E	0.026	1.10	0.056	0.0013	-0.23	17.80	1611.3	232.9	2.15
PS	Ref	0.036	0.90	0.013	0.0026	0.20	-0.46	208.1	95.3	2.26
	Case A	0.023	0.86	0.009	0.0011	0.21	-1.62	237.8	42.1	2.83
	Case B	0.021	0.89	0.033	0.0009	0.22	-3.15	442.5	136.3	2.38
	Case C	0.013	0.90	0.049	0.0003	0.22	-16.63	806.5	127.5	2.46
	Case D	0.036	0.90	0.013	0.0026	0.21	-0.42	205.4	93.8	2.28
	Case E	0.025	0.85	0.008	0.0013	0.19	-1.27	207.2	40.1	2.78

Table 3: Integral quantities of streamwise development of turbulent boundary layer over suction (SS) and pressure side (PS) obtained at $x/c = 0.75$.

Figs. 8(a) and 8(c) depict the inner-scaled mean wall-tangential velocity on the suction side and pressure side at $x/c = 0.75$, respectively. Note that the development of log-layer is less pronounced due to the low-Reynolds-number effects (Vinuesa et al., 2018). Uniform suction significantly modifies the inner-scaled profile on the suction side, attenuating the wake region by approximately 50%, 40%, and 28% for Cases A, B, and C, respectively. The undershooting of log-layer becomes more evident with increasing control intensity (ψ). Within the buffer layer, the profiles shift downward toward the wall, with Cases A, B, and C aligning closely.

On the pressure side, uniform blowing has the opposite impact, intensifying U_t^+ in the overlap and wake regions. Regardless of the deviations in the wake region, the profiles of Case D on the suction side and E on the pressure side align well with that of Case A. Note that Cases B and C exhibit a slight dip near the potential region, which is caused by excessive control intensity.

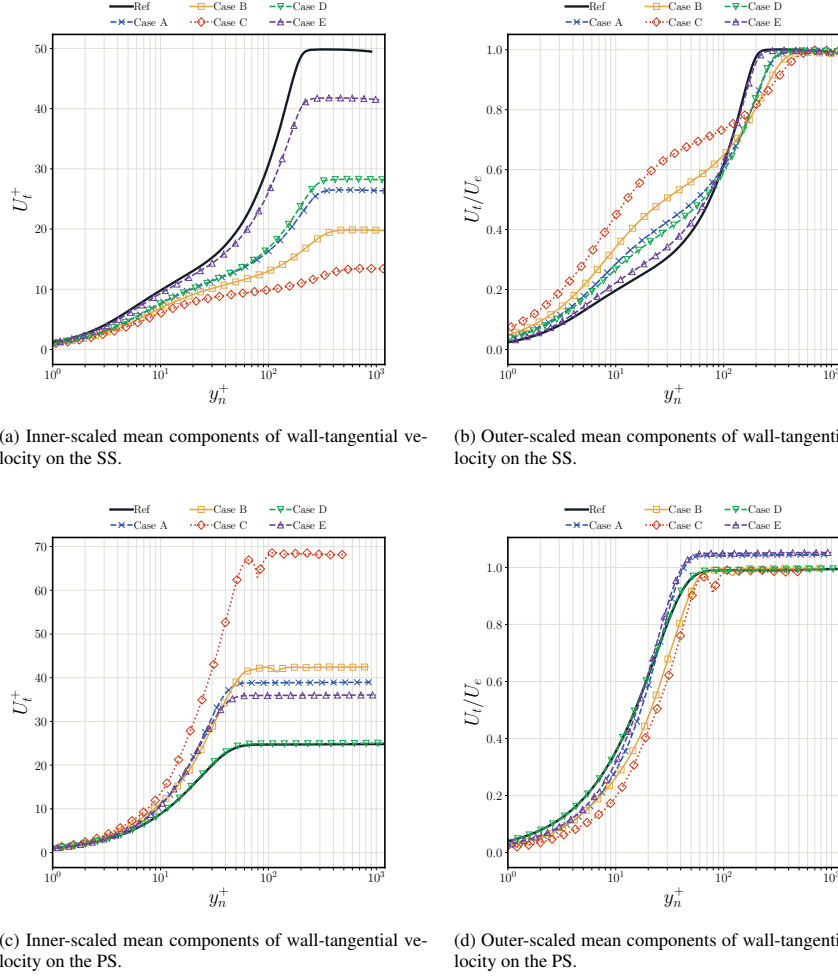


Figure 8: (a, c) Inner- and (b, d) outer-scaled mean components of wall-tangential velocity (U_t) as a function of inner-scaled wall-normal distance (y_n^+) on the (a, b) suction and (c, d) pressure side at streamwise location of $x/c = 0.75$, respectively. The color code follows tab. 1.

The control effects on U_t are further revealed by evaluating the outer-scaled profiles, which are demonstrated in figs. 8(b) and 8(d). The wake regions of all cases collapse, indicating that inner-scaled wake modifications are due to changes in u_τ . The results also suggest that the deviation between profiles of Case D/E and A on the suction/pressure side is caused by the variation of u_τ . The overlap region of controlled profiles overshoot the log-layer, being opposite to the inner-scaled profiles. Additionally, within the buffer layer, controlled profiles exhibit higher magnitudes, where the variations are proportional to ψ .

Adverse pressure gradient (APG) and FPG decelerate and accelerate TBL development, respectively, significantly impacting the wall-normal velocity (V_n). Fig. 9 depicts the inner- and outer-scaled V_n profiles at $x/c = 0.75$. On the suction side, uniform suction significantly attenuates V_n , with the effect increasing with wall-normal distance and control intensity. On the pressure side, uniform blowing intensifies V_n by increasing the wall-normal convection, being similar to the effect of strong APGs. Interestingly, the profiles of Cases A and B align closely in the wake region, while Case C deviates due to distinct differences in β at this location (-1.62 , -3.15 , and -16.63 for Cases A, B, and C, respectively). The profiles of Case D on the suction and Case E on pressure side deviate with respect to that of Case A, which is evident for inner- and outer-scaled profiles, being connected to the variation of β . Note that the sink observed in U_t profiles on the pressure side is also present in V_n profiles. Moreover, the magnitude of controlled V_n/U_e at the wall matches the imposed boundary conditions described in § 2.2, validating the implementation.

Apart from the mean-velocity profiles, we assess the Reynolds stresses to investigate the momentum distribution along the wall-normal direction, which is critical to understand the control effects. Figs. 10(a) and 10(b) depict the inner- and outer-scaled Reynolds stress profiles at $x/c = 0.75$ on the suction side, respectively. The reference case ($\beta = 27.97$ for the reference case) exhibit an outer peak in the overlap region for the $\overline{u_t^2}$ profiles, being more prominent than the inner peak in the buffer layer, which is pronounced in both inner- and outer-scaled profiles. Uniform suction significantly attenuates both peaks and intensifies the wake region. The modified $\overline{u_t^2}/U_e^2$ profiles exhibit intensified inner and outer peaks, indicating that the effects are primarily due to modifications in u_τ , while the prominent wake region of modified $\overline{u_t^2}/U_e^2$ remains pronounced, being evident for inner- and outer-scaled profiles.

It is worth noting that, at lower AoA (5°), Atzori et al. (2020) reported that uniform suction enhances the inner peak while suppressing the outer peak by adopting a similar input intensity $\psi = 0.2\%$ with the same control area. The major discrepancy is attributed to the larger β in the present study ($\beta = 27.97$ vs. $\beta = 6.6$), which is nearly five times higher. This suggests that high β significantly influences the control performance.

On the pressure side, $\overline{u_t^2}$ profiles exhibit low magnitudes of $\sim O(10^{-3})$ due to low Reynolds numbers and strong FPGs. Uniform blowing significantly intensifies $\overline{u_t^2}$ with substantially high magnitude, producing a peak in the overlap region, which is pronounced for inner- and outer-scaled profiles. Additionally, Cases B and C exhibit a similar buffer-layer response, being consistent with the observations in Atzori et al. (2020).

Moreover, the outer-scaled profiles of Case E produces a less prominent outer peak than that of Case A on the pressure side, which is connected to the variation of u_τ . On the contrary, the Case D produces a more prominent outer peak than that of Case A on the suction side, while the inner peaks of both profiles are collapsed. At this location, Case D achieves a lower β than Case A on the suction side. Therefore, the results implies that control effectiveness depends on flow history and β variations (Atzori et al., 2021; Pozuelo et al., 2022; Wang et al., 2024).

Regarding other Reynolds stresses, namely the fluctuation components of wall-tangential ($\overline{v_n^2}$) and spanwise ($\overline{w^2}$) velocity as well as the Reynolds-shear stress ($\overline{u_t v_n}$), the modifications are simpler to describe than that of $\overline{u_t^2}$. On the suction side, due to the increased wall-normal convection caused by strong APGs, the wall-normal position of the outer peaks align with that of $\overline{u_t^2}$ in the overlap region. The effects of uniform suction vary with the wall-normal distance. In particular, below the wall-normal plane of the outer peak, uniform suction remarkably attenuates

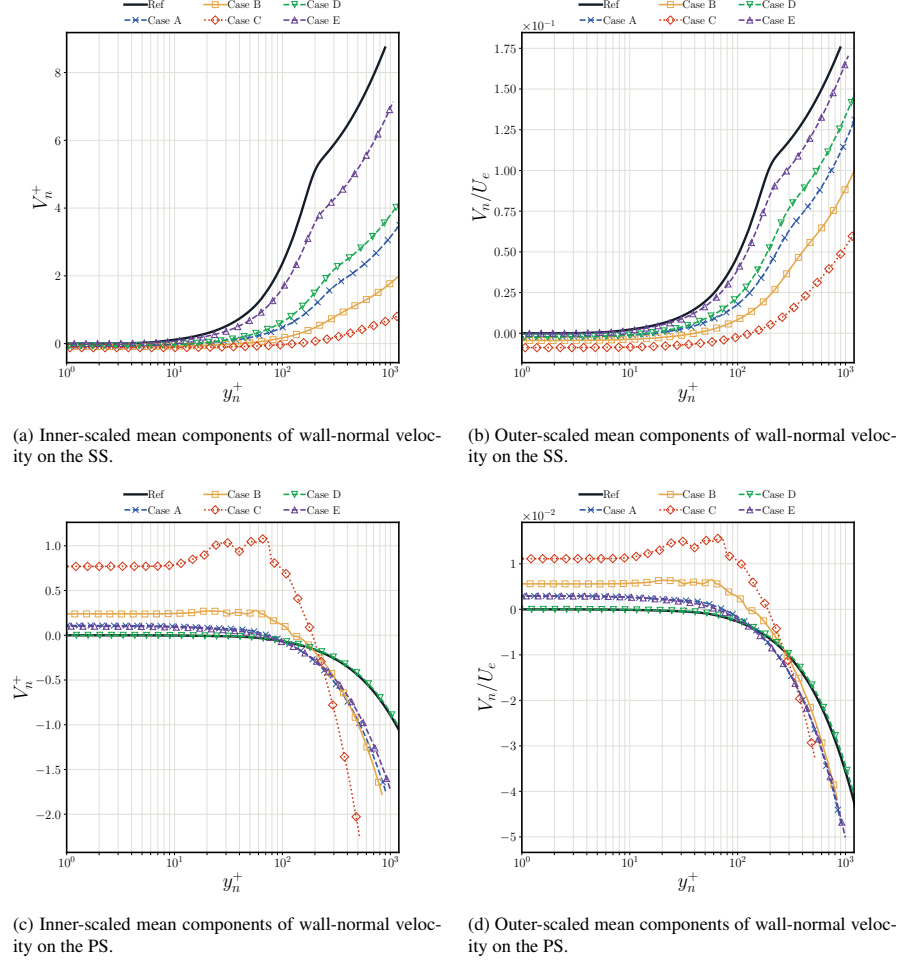


Figure 9: (a, c) Inner- and (b, d) outer-scaled mean components of wall-normal velocity (V_n) as a function of inner-scaled wall-normal distance (y_n^+) on the (a, b) suction and (c, d) pressure side at streamwise location of $x/c = 0.75$, respectively. The color code follows tab. 1.

the $\overline{v_n^2}$, $\overline{w^2}$ and $\overline{u_t v_n}$, which is observed for both inner- and outer-scaled profiles. Above this wall-normal position, the uniform suction intensifies the profiles of Reynolds stresses, which can be more clearly observed on the outer-scaled profiles in fig. 10(b).

On the other hand, uniform blowing on the pressure side significantly intensifies the $\overline{v_n^2}$ and $\overline{u_t v_n}$ values within the inner region, while the modification on $\overline{w^2}$ is very negligible. Note that the intensified $\overline{v_n^2}$ exhibits an outer peak at a wall-normal position that is farther from the wall compared to the one of $\overline{u_t^2}$.

Additionally, to evaluate the control mechanism in terms of momentum exchange, we assess the visualization of vortical structures identified using the λ_2 method (Jeong and Hussain, 1995). Fig. 11 shows isosurfaces of these structures, colored by streamwise velocity. The region of

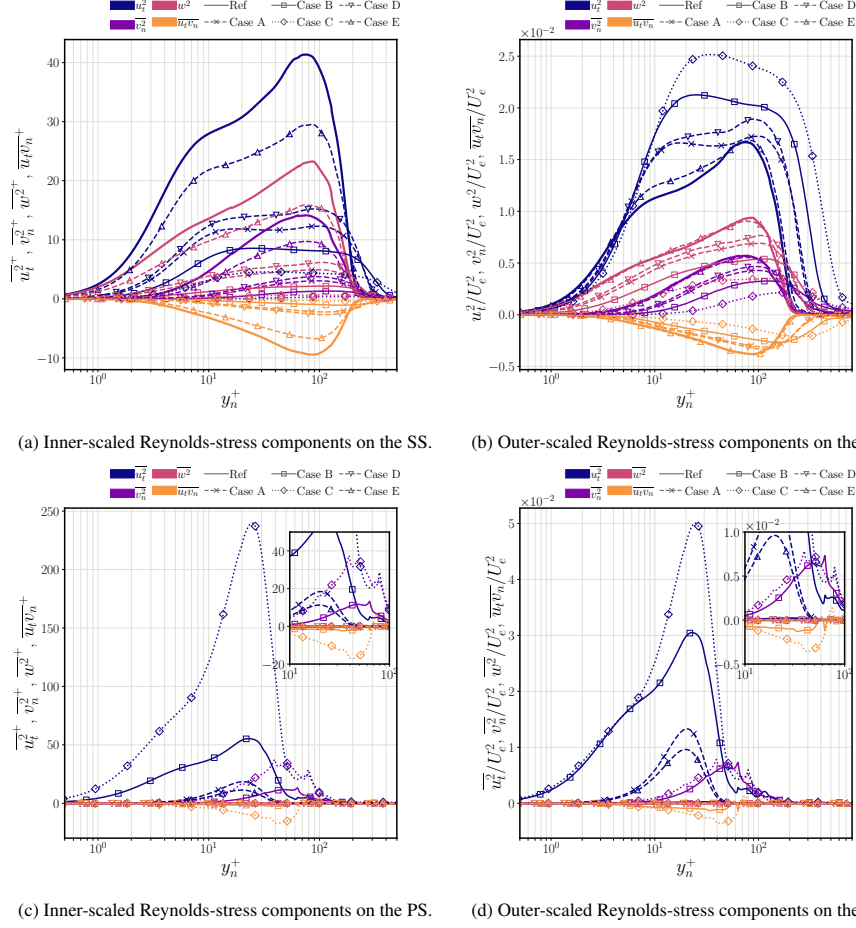


Figure 10: ((a), (c)) Inner- and ((b), (d)) outer-scaled fluctuation components of wall-tangential ($\overline{u_t^2}$), wall-normal ($\overline{v_n^2}$) and spanwise ($\overline{w^2}$) velocity as well as Reynolds-shear stress ($\overline{u_t v_n}$) as a function of inner-scaled wall-normal distance (y_n^+) on the ((a), (b)) suction and ((c), (d)) pressure side at streamwise location of $x/c = 0.75$, respectively.

interest spans from $x/c = 0.5$ to 1.5 , encompassing the separated flow region and the near-wake area downstream of the TE.

The control effect on momentum exchange becomes evident when examining the spatial development of high- and low-speed regions along the wing surface. Under uniform suction applied to the SS, both the off-wall high-speed regions and near-wall low-speed regions are attenuated as suction intensity increases. This behavior is attributed to the mechanism by which steady suction removes low-momentum fluid and redirects high-momentum fluid toward the wall. Consequently, the regions with the lowest streamwise velocity (i.e., shown in dark blue) are significantly reduced, which corresponds to delayed separation. On the other hand, uniform blowing on the PS generates near-wall vortical structures by enhancing wall-normal momentum transfer. This displaces near-wall flow to the outer region and becomes more pronounced with increasing control intensity, consistent with the observation shown in fig. 10(d).

Interestingly, Cases B and C also exhibit a remarkable impact on the vortex shedding in the near wake, with a dramatic modification of flow structures. This is likely due to the combined effects of the control type and intensity, as such changes are not observed when applying a lower intensity ($\psi = 0.25\%$) or using either uniform suction or blowing alone.

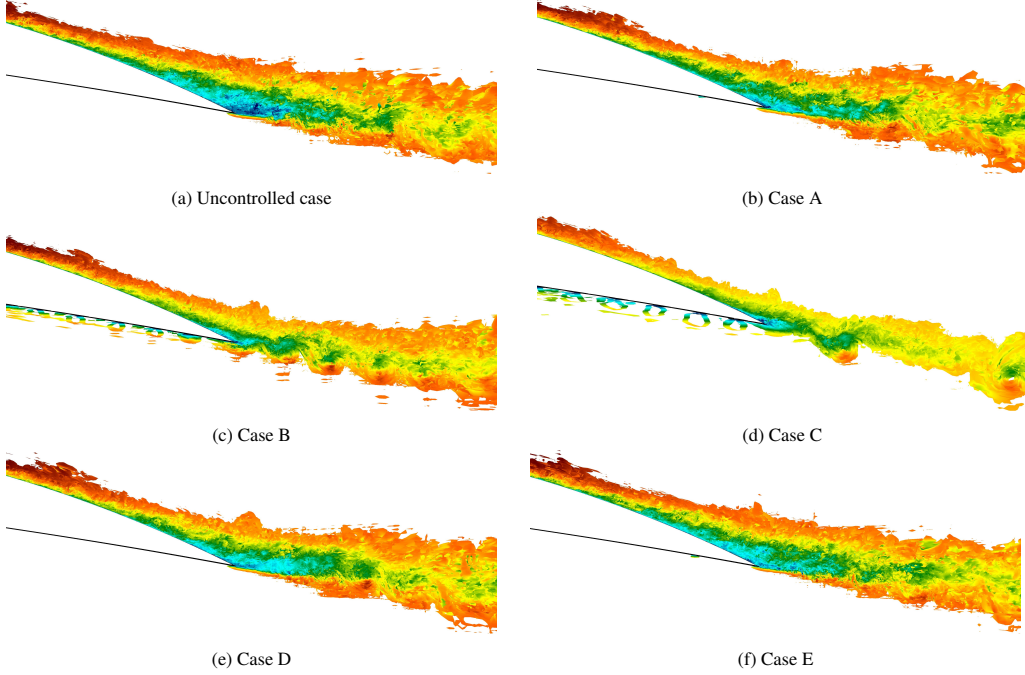


Figure 11: Visualization of vortical structures identified by the λ_2 method (Jeong and Hussain, 1995) between $x/c = 0.5$ and 1.5 , colored by the instantaneous streamwise velocity at an arbitrary time step. An isosurface of $\lambda_2 = -10$ is shown in all the cases. The vortical motions are colored by their streamwise velocity value, ranging from $-0.4U_\infty$ (dark blue) to $1.6U_\infty$ (dark red).

3.4. Time-series analysis

In this section, we employ the spectral analysis to investigate the temporal and scale-dependent interactions between control and TBLs. To this end, time series of the velocity components and pressure were collected for multiple wall-normal profiles across various streamwise locations, extending to $x/c = 1.74$ in the wake. The dataset spans a total of 2 flow-over times after excluding initial transients, with a sampling rate of 2×10^{-4} flow-over times.

First, we assess the one-dimensional power-spectral densities (PSDs) computed using the fast Fourier transform (FFT). Fig. 12 depicts the contours of the inner-scaled premultiplied PSD of wall-tangential velocity fluctuations ($k_z \phi_{u_i u_i}^+$) at $x/c = 0.75$ on the suction side, expressed as a function of inner-scaled spanwise wavelength λ_z^+ and wall-normal distance y_n^+ . Under strong APG conditions near separation, the wall-normal profile of $\overline{u_i^2}$ (see fig. 10) reveals that the outer peak in the overlap region dominates over the inner peak in the buffer layer. Spectral analysis confirms the absence of the inner peak (typically at $\lambda^+ \approx 100$), which is typically present in canonical wall-bounded flows and lower angles of attack ($AoA = 5^\circ$) (Atzori et al., 2021; Wang

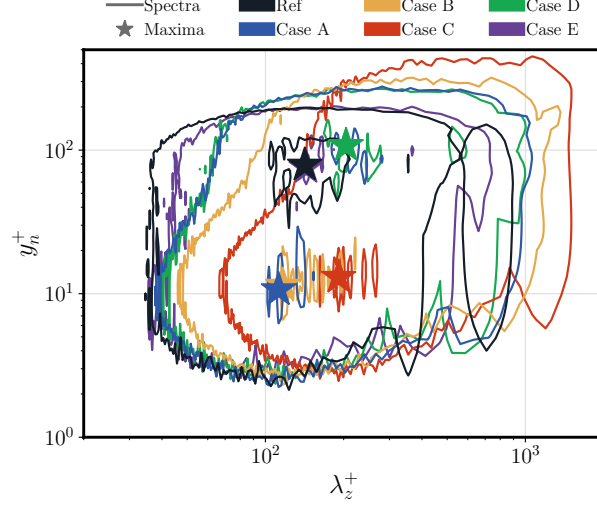


Figure 12: Inner-scaled premultiplied spanwise power-spectral density (PSD) of the wall-tangential velocity fluctuation, in terms of the inner-scaled spanwise wavelength (λ_z^+) and wall-normal distance (y_n^+) at $x/c = 0.75$ on the suction side. The contours illustrate the levels corresponding to 20% and 80% of the maximum power density, whereas the locations of the maxima achieved are marked with stars. The color code follows tab. 1.

et al., 2024; Mallor et al., 2024b). Instead, the outer peak of small-scale structures dominates the energy distribution, highlighting the strong influence of increased wall-normal convection due to APGs.

Uniform suction over the suction side significantly modifies the energy distribution under near-separation conditions. By introducing high-momentum fluid near the wall, the energy peak shifts toward the buffer layer, and small-scale structures in the overlap region are attenuated, restoring characteristics of the canonical near-wall cycle. Cases A, B, and C shift the energy peak to $y_n^+ = 10.6$, 11.5 , and 13.0 , respectively, compared to $y_n^+ = 78.7$ in the uncontrolled case. Additionally, Case A and B yield smaller wavelengths ($\lambda_z^+ = 112$ and 116) compared to the reference ($\lambda_z^+ = 141$), while Case C shifts toward a larger wavelength ($\lambda_z^+ = 191$). Uniform suction also enhances large-scale structures in the outer region, with effects increasing with ψ .

The spectra of Cases D and E deviate from their combined counterpart (Case A). Case D shifts the outer peak further from the reference instead of producing an inner peak, while Case E introduces minimal modification. However, Case E attenuates small-scale structures in the overlap region and enhances large-scale energy in the outer region. The results indicate that those modifications are due to the variation of u_τ .

Next, we examine the PSDs of the fluctuating streamwise velocity (u) and pressure (p) in the wake to analyze control effects on vortex-shedding frequency. Time-series data were collected at $x/c = 1.5$ and 1.74 , at a vertical position of $y = 0$. Note that this region corresponds to the vortex-formation zone, where the downstream energy evolution of vortex shedding can be effectively captured (Yarusevych et al., 2009). Moreover, previous studies on airfoil wakes (Gerontakos and Lee, 2005; Yarusevych et al., 2009; Liu et al., 2017) have employed similar measurement positions within comparable Reynolds number regimes. Therefore, the current results may serve

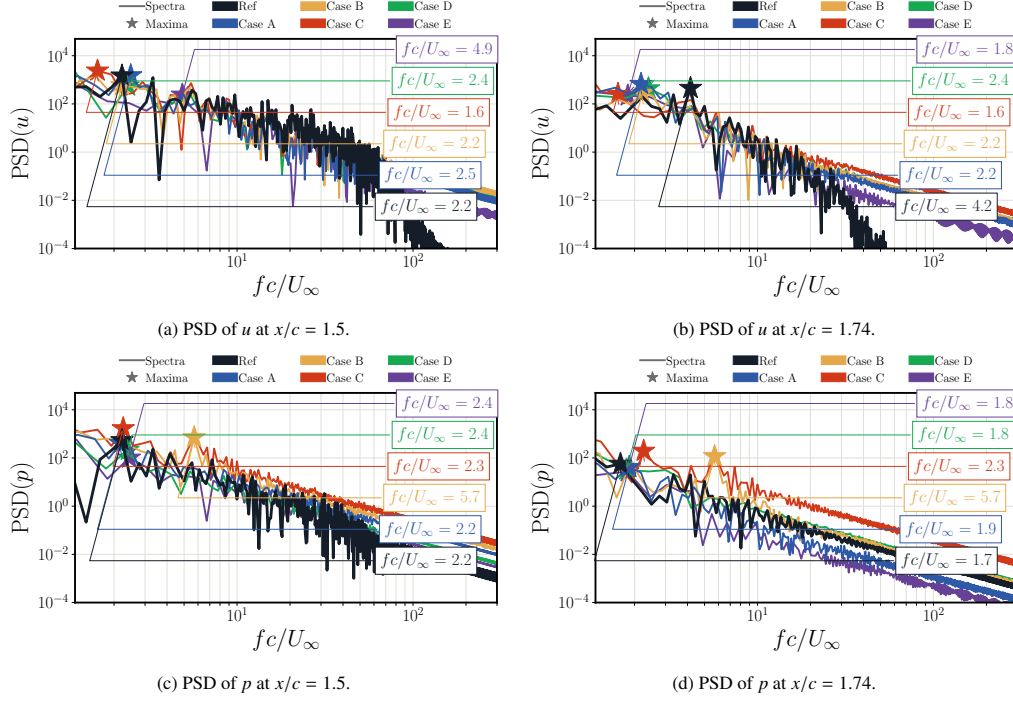


Figure 13: Power-spectral density (PSD) of ((a), (b)) fluctuating streamwise velocity and ((c), (d)) pressure in terms of the dimensionless frequency (fc/U_∞) measured at streamwise location x/c of ((a), (c)) 1.5 and ((b), (d)) 1.74, respectively, where the locations and value of the dominant frequencies are marked with stars and denoted by panels, respectively. The color code follows tab. 1.

as a useful reference for future investigations.

Figs. 13(a) and 13(b) depict the PSDs of u as a function of the dimensionless frequency fc/U_∞ at $x/c = 1.5$ and 1.74. In the uncontrolled case, the vortex-shedding frequency increases downstream, rising from $fc/U_\infty = 2.2$ at $x/c = 1.5$ to 4.2 at $x/c = 1.74$, which is consistent with Yarusevych et al. (2009). Control using combined uniform suction and blowing results in minor modifications to the vortex-shedding frequency. Cases A, B, and C yield fc/U_∞ values of 2.5, 2.2, and 1.6 at both locations, closely matching the uncontrolled case. However, the effects of applying suction or blowing individually vary with the streamwise location. Case D exhibits an increased dominant frequency ($fc/U_\infty = 2.4$), similar to Case A at both locations, whereas Case E results in $fc/U_\infty = 4.9$ and 1.8 at $x/c = 1.5$ and 1.75, respectively. Additionally, all configurations amplify the PSD values for high-frequency components, which is particularly evident in fig. 13(b). For the pressure spectra (Figs. 13(c) and 13(d)), the dominant frequency slightly decreases downstream, being $fc/U_\infty = 2.2$ and 1.7 at $x/c = 1.5$ and 1.74, respectively. Similarly, the modified fc/U_∞ exhibits a downstream reduction, while its deviation from the reference is minimal except in Case B, where the dominant frequency drastically increases to $fc/U_\infty = 5.7$. Interestingly, the dominant frequency of Case B resonates with that of the secondary peak of Case C, which is not observed in other configurations, suggesting a significant modification of the wake due to high control intensity. However, the modifications to the

high-frequency spectra of the PSDs vary with the streamwise location. While all configurations energize the high-frequency motions at $x/c = 1.5$, only Case C exhibits a significantly energized spectrum at $x/c = 1.74$. These results highlight the crucial role of control intensity in modifying the vortex-shedding frequency.

4. Summary and conclusions

In the present study, we investigated the effects of various separation-control approaches on a NACA4412 wing section at an angle of attack (AoA) of 11° and a Reynolds number of $Re_c = 200,000$. High-resolution large-eddy simulations (LESs) were carried out using the spectral-element-method solver Nek5000 (Fischer et al., 2008), incorporating adaptive mesh refinement (AMR) for non-conformal meshes. This approach enables the use of a wide spanwise width ($L_z = 0.6$) while maintaining high accuracy, ensuring the capture of large-scale structures and accurate resolution of flow separation.

A range of control configurations were considered, categorized as follows: (1) uniform suction on the suction side, (2) uniform blowing on the pressure side, (3) combined uniform suction and blowing, and (4) periodic control on the suction side. The control impact on aerodynamic characteristics, including separation length (ℓ_{sep}), lift, drag components, and aerodynamic efficiency, was evaluated. Note that control intensities (ψ) and control areas were chosen based on previous studies (Atzori et al., 2020; Mallor et al., 2024a).

Overall, the tested uniform blowing and/or suction strategies facilitated flow reattachment but had varying effects on aerodynamic efficiency. Specifically, uniform suction alone produced the same reduction in ℓ_{sep} as combined suction and blowing, but resulted in a smaller lift increase while causing similar drag increases, leading to a larger decrease in aerodynamic efficiency. Notably, uniform blowing on the pressure side was the only configuration that improved aerodynamic efficiency, albeit with a smaller reduction in ℓ_{sep} . The control effects on aerodynamic characteristics differed significantly from previous studies at lower AoA (Atzori et al., 2020) and higher Reynolds numbers (Mallor et al., 2024a). Furthermore, adjustments to control configurations did not yield additional benefits, and periodic control (§ Appendix A) neither further delayed separation nor improved aerodynamic efficiency.

These findings motivated an in-depth investigation of the interaction between control and turbulent boundary layers (TBLs) over the wing section. Control significantly modified the skin-friction coefficient (c_f) and pressure coefficient (c_p). Uniform suction increased both c_f and c_p , while uniform blowing reduced c_f but increased c_p , consistent with findings at $AoA = 5^\circ$ (Atzori et al., 2021; Fahland et al., 2023). The effects on c_p were equivalent to increasing the angle of attack. Further analysis of the Clauser pressure-gradient parameter (β) showed that uniform suction attenuated boundary-layer development by reducing β and momentum thickness (θ), whereas uniform blowing on the pressure side exhibited effects dependent on control intensity.

Turbulence statistics at $x/c = 0.75$ were examined on both airfoil surfaces. The control effects on mean wall-tangential and wall-normal velocity profiles were consistent with previous studies at $AoA = 5^\circ$ (Atzori et al., 2020). However, modifications to the streamwise velocity fluctuations ($\overline{u_t^2}$) on the suction side differed: uniform suction intensified the outer peak in the overlap region rather than attenuating it, influenced by strong adverse pressure gradients and flow history. On the pressure side, strong favorable pressure gradients (FPGs) produced Reynolds stresses with low magnitudes, whereas uniform blowing significantly increased wall-tangential fluctuations and Reynolds shear stress.

Spectral analysis further reveals the control effects on $\overline{u_t^2}$. One-dimensional power-spectral density (PSD) analysis at $x/c = 0.75$ revealed that uniform suction energized large-scale structures in the outer layer and small-scale structures in the buffer layer. Notably, an inner peak emerged only when suction was combined with uniform blowing. Additionally, PSD analysis of fluctuating streamwise velocity and pressure in the wake showed that control significantly reduced the vortex-shedding frequency.

An important avenue for future research is exploring control performance across a broader range of AoA to provide a more general understanding. Comparing results at $AoA = 5^\circ$ and 11° highlighted difference in control effects, suggesting that the need for further investigation. However, the present study focused on a specific AoA to validate and compare against the configuration proposed by [Mallor et al. \(2024a\)](#), making broader investigations beyond the current scope.

A key challenge is optimizing control schemes to simultaneously improve aerodynamic efficiency and delay flow separation. Our results show that separation is delayed, but aerodynamic efficiency is reduced. Neither modifying configurations nor employing periodic control improved L/D (§ [Appendix A](#)). One possible explanation is that flow separation in this case is less pronounced compared to near-stall conditions at higher AoA (e.g., $\ell_{sep} = 0.51$ at $AoA = 14^\circ$ for higher Re_c ([Mallor et al., 2024b](#))), where lift improvement outweighs drag penalties. However, this reasoning does not apply to the current case, where most of the flow remains attached. Achieving a balance between separation delay and aerodynamic efficiency is challenging, as separation control inherently involves increasing near-wall momentum ([Greenblatt and Wygnanski, 2000](#)), which inevitably leads to higher drag.

Deep reinforcement learning (DRL) could offer a potential solution to the challenges faced by traditional control methods. As discussed in § 1, DRL can identify complex flow conditions and generate optimal responses to maximize objectives (e.g., delaying separation and improving L/D) by leveraging neural networks to approximate nonlinear functions ([Vinuesa et al., 2022](#)). In the context of separation control, [Suárez et al. \(2024a\)](#) demonstrated that DRL can enhance aerodynamic efficiency while reducing energy consumption.

In summary, this study provides a comprehensive analysis of separation-control interactions with turbulent boundary layers over a wing section. To the authors' best knowledge, this is the first numerical study utilizing high-resolution LESs to provide comprehensive assessments on separation control.

Data availability

The data that support the findings of this study will be openly available on GitHub-[KTH-FlowAI](#) after publication.

Competing interesting

The authors declare that they have no competing interests.

Acknowledgements

Numerical studies were enabled by resources provided by the National Academic Infrastructure for Supercomputing in Sweden (NAISS) at PDC center for High Performance Computing

in KTH (stockholm). RV acknowledges the financial support from ERC grant no. ‘2021-CoG-101043998, DEEPCONTROL’. Views and opinions expressed are those of the authors only and do not necessarily reflect those of the European Union or the European Research Council. Neither the European Union nor the granting authority can be held responsible for them.

CRedit authorship contribution statement

YW: Methodology, Software, Validation, Investigation, Data curation, Data generation, Writing - Original Draft, Writing - Review & Editing, Visualization. FM: Methodology, Software, Validation, Investigation, Data curation, Data generation, Writing - Original Draft, Writing - Review & Editing. CGG: Ideation, Methodology, Validation, Investigation, Data generation, Writing - Original Draft, Writing - Review & Editing. RM: Writing - Review & Editing. RV: Ideation, Methodology, Validation, Data generation, Writing - Original Draft, Writing - Review & Editing, Resources, Funding acquisition.

Declaration on artificial-intelligence (AI) assistance

This paper has benefited from AI-assisted language refinement. Specifically, ChatGPT was employed for polishing the text, improving readability, and ensuring clarity. However, the conceptual development, data analysis, and conclusions presented in this work are the sole responsibility of the authors.

Appendix A. Aerodynamic effects of periodic control and uniform suction over suction side

In this section, we report the aerodynamic characteristics obtained from applying (1) periodic control and (2) uniform suction over the suction side with various configurations. Periodic control is a well-established separation control approach that introduces periodic excitation to modify the spreading rate of the mixing layer (Greenblatt and Wygnanski, 2000), with successful applications in various studies (Kim et al., 2007; Gul et al., 2014; Tang et al., 2014; Çetin et al., 2018; Wu et al., 2022). It is typically applied near the separation point within a limited control area.

We first examined the potential of periodic control in delaying separation. The control was implemented as a Dirichlet boundary condition at the wall, with the imposed control input defined as:

$$V_{n,w} = \psi \sin(2\pi F^* t), \quad (\text{A.1})$$

where ψ represents the input intensity, while F^* and t denote the dimensionless control frequency and flow-over time, respectively. The imposed control velocity $V_{n,w}$ is directed wall-normal but is decomposed into horizontal and vertical components to ensure a combined magnitude equal to $V_{n,w}$. Note that the choice of F^* depends on the vortex-shedding frequency but is not strictly bounded to it. In addition to $F^* = 4.2$ (i.e., the vortex-shedding frequency at $x/c = 1.74$), we select various F^* values such that $F^* \sim 1$, which is suggested as the optimal frequency for separation control (Mabey, 1972; Roshko, 1985; Hsiao et al., 1990; Amitay et al., 2001; Tuck and Soria, 2008). This optimal frequency is independent of curvature and the state of the separating boundary layer (Greenblatt and Wygnanski, 2000). Additionally, $F^* = 10.10$ is test to explore the performance of high-frequency control.

Name	ℓ_{sep}	$C_{\mu}[\times 10^{-5}]$	C_l	$C_{d,p}$	$C_{d,f}$	$C_d = C_{d,p} + C_{d,f}$	L/D	F^*	ψ [% U_{∞}]	Control area [x/c]
Ref	0.14	0.0	1.314	0.0450	0.0078	0.052	24.88	—	—	—
Case 1	0.06 (−57%)	0.012	1.310 (−0.30%)	0.0470 (+4.49%)	0.0077 (−0.77%)	0.054 (+3.71%)	23.91 (−3.90%)	1.0	0.1	0.80 ~ 0.86
Case 2	0.05 (−64%)	0.012	1.304 (−0.76%)	0.0461 (+2.47%)	0.0078 (−0.26%)	0.054 (+2.06%)	24.19 (−2.77%)	4.2	0.1	0.80 ~ 0.86
Case 3	0.05 (−64%)	0.012	1.308 (−0.46%)	0.0468 (+4.09%)	0.0078 (−0.38%)	0.055 (+3.43%)	23.95 (−3.74%)	0.86	0.1	0.80 ~ 0.86
Case 4	0.05 (−64%)	0.012	1.308 (−0.46%)	0.0468 (+4.09%)	0.0078 (−0.51%)	0.055 (+3.41%)	23.95 (−3.74%)	10.10	0.1	0.80 ~ 0.86
Case 5	0.05 (−64%)	1.2	1.299 (−1.14%)	0.0451 (+0.31%)	0.0078 (−0.26%)	0.053 (+0.23%)	24.55 (−1.33%)	0.63	1.0	0.86 ~ 0.92
Case 6	0.05 (−64%)	1.2	1.308 (−0.46%)	0.0468 (+4.09%)	0.0078 (−0.38%)	0.055 (+3.43%)	23.95 (−3.74%)	0.94	1.0	0.86 ~ 0.92
Case 7	0.05 (−64%)	1.2	1.301 (−0.99%)	0.0454 (+0.87%)	0.0078 (−0.38%)	0.053 (+0.68%)	24.46 (−1.69%)	0.94	1.0	0.86 ~ 0.92
Case 8	0.05 (−64%)	2.8	1.309 (−0.38%)	0.0480 (+6.71%)	0.0079 (+1.02%)	0.056 (+5.87%)	23.42 (−5.87%)	1.16	1.0	0.86 ~ 1.00
Case 9	0.04 (−71%)	11.2	1.314 (0.00%)	0.0478 (+6.25%)	0.0078 (−0.51%)	0.056 (+5.25%)	23.63 (−5.03%)	1.16	2.0	0.86 ~ 1.00

Table A.4: Separation length (ℓ_{sep}), momentum coefficient (C_{μ}), lift coefficient (C_l), drag components ($C_{d,p}$ and $C_{d,f}$), total drag (C_d), and aerodynamic efficiency (L/D) for periodic control cases on suction side of a NACA4412 airfoil at $AoA = 11^\circ$ and $Re_c = 200,000$. Percent changes from the reference case are shown in parentheses. The values in the parentheses report the relative changes obtained by control. The F^* denotes the input frequency of control.

Tab. A.4 summarizes the aerodynamic efficiency and separation delay for the periodic control cases. Although periodic control effectively delays separation, it generally reduces lift (except for Case 9) and increases drag, leading to a decline in aerodynamic efficiency. Notably, friction drag is slightly reduced, while pressure drag increases significantly due to control application.

We also conducted additional tests to examine the effect of uniform suction over the suction side, specifically investigating the impact of control area location, which is typically adjacent to the separation point (Carnarius et al., 2007; Azim et al., 2015; Oktay and Kanat, 2019). A broader range of input intensities ψ , up to $7.5\%U_{\infty}$, was also explored. Tab. A.5 summarizes the aero-

Name	ℓ_{sep}	$C_{\mu}[\times 10^{-5}]$	C_l	$C_{d,p}$	$C_{d,f}$	$C_d = C_{d,p} + C_{d,f}$	L/D	ψ [% U_{∞}]	Control area [x/c]
Ref	0.14	—	1.314	0.0450	0.0078	0.052	24.88	—	—
Case 1	0.06 (−57%)	0.6	1.314 (0.00%)	0.0477 (+6.11%)	0.0080 (+2.30%)	0.056 (+5.55%)	23.58 (−5.23%)	0.50	0.80 ~ 0.92
Case 2	0.06 (−57%)	0.012	1.311 (−0.23%)	0.0472 (+4.91%)	0.0078 (−0.77%)	0.055 (+4.09%)	23.85 (−4.14%)	0.10	0.86 ~ 0.92
Case 3	0.06 (−57%)	0.3	1.311 (−0.23%)	0.0474 (+5.34%)	0.0078 (−0.51%)	0.055 (+4.47%)	23.77 (−4.46%)	0.50	0.86 ~ 0.92
Case 4	0.05 (−64%)	1.2	1.314 (0.00%)	0.0479 (+6.54%)	0.0078 (−0.38%)	0.056 (+5.51%)	23.59 (−5.18%)	1.00	0.86 ~ 0.92
Case 5	0.03 (−78%)	30.0	1.320 (+0.46%)	0.0490 (+9.03%)	0.0079 (+0.26%)	0.057 (+7.71%)	23.21 (−6.71%)	5.00	0.86 ~ 0.92
Case 6	0.05 (−64%)	30.0	1.334 (+1.52%)	0.0520 (+15.50%)	0.0078 (+0.13%)	0.060 (+13.22%)	22.31 (−10.33%)	5.00	0.86 ~ 0.92
Case 7	0.05 (−64%)	11.2	1.334 (+1.52%)	0.0520 (+15.50%)	0.0078 (+0.13%)	0.060 (+13.22%)	22.31 (−10.33%)	2.00	0.86 ~ 1.00
Case 8	0.03 (−78%)	70.0	1.374 (+4.57%)	0.0600 (+33.73%)	0.0080 (+1.92%)	0.068 (+29.00%)	20.17 (−18.93%)	5.00	0.86 ~ 1.00
Case 9	0.03 (−57%)	78	1.432 (+8.98%)	0.0700 (+55.31%)	0.0089 (+13.41%)	0.079 (+49.04%)	18.20 (−26.85%)	7.50	0.86 ~ 1.00

Table A.5: Separation length (ℓ_{sep}), momentum coefficient (C_{μ}), lift coefficient (C_l), drag components ($C_{d,p}$ and $C_{d,f}$), total drag (C_d), and aerodynamic efficiency (L/D) for uniform suction control cases on the suction side of a NACA4412 airfoil at $AoA = 11^\circ$ and $Re_c = 200,000$. Percent changes from the reference case are shown in parentheses. The values in the parentheses report the relative changes obtained by control.

dynamic efficiency and separation delay for uniform suction cases. Generally, uniform suction increases lift, increases total drag, and delays separation, consistent with the results presented in section 3. However, applying suction adjacent to the separation point does not necessarily enhance aerodynamic efficiency or further delay separation.

References

- E. Maskell, Flow separation in three dimensions, RAE Report No. Aero 2565 (1955).
- R. L. Simpson, Turbulent boundary-layer separation, Annual Review of Fluid Mechanics 21 (1989) 205–232.
- S. Abdollahipour, Review on flow separation control: effects of excitation frequency and momentum coefficient, Frontiers in Mechanical Engineering 10 (2024) 1380675. doi:10.3389/fmech.2024.1380675.
- K. Fukagata, K. Iwamoto, Y. Hasegawa, Turbulent drag reduction by streamwise traveling waves of wall-normal forcing, Annual Review of Fluid Mechanics 56 (2024) 69–90.
- D. Greenblatt, I. J. Wygnanski, The control of flow separation by periodic excitation, Progress in Aerospace Sciences (2000).

- M. Gad-el Hak, Modern Developments in Flow Control, *Applied Mechanics Reviews* 49 (1996) 365–379. URL: <https://doi.org/10.1115/1.3101931>. doi:10.1115/1.3101931.
- J. C. Lin, Review of research on low-profile vortex generators to control boundary-layer separation, *Progress in aerospace sciences* 38 (2002) 389–420.
- C. Neves, R. Mariani, Flow control on a swept wing using aerodynamically shaped vortex generators, in: *AIAA SCITECH 2024 Forum*, 2024, p. 0140.
- M. Amitay, D. R. Smith, V. Kibens, D. E. Parekh, A. Glezer, Aerodynamic flow control over an unconventional airfoil using synthetic jet actuators, *AIAA Journal* 39 (2001) 361–370. doi:10.2514/2.1323.
- S. L. Brunton, B. R. Noack, Closed-Loop Turbulence Control: Progress and Challenges, *Applied Mechanics Reviews* 67 (2015) 050801. doi:10.1115/1.4031175.
- B. Nishri, I. Wygnanski, Effects of periodic excitation on turbulent flow separation from a flap, *AIAA journal* 36 (1998) 547–556.
- L. Huang, L. Maestrello, T. Bryant, Separation control over an airfoil at high angles of attack by soundemanating from the surface, in: *19th AIAA, Fluid Dynamics, Plasma Dynamics, and Lasers Conference*, 1987, p. 1261.
- P. Suárez, F. Alcántara Ávila, A. Miró, J. Rabault, B. Font, O. Lehmkuhl, R. Vinuesa, Active flow control for drag reduction through multi-agent reinforcement learning on a turbulent cylinder at $Re_D = 3900$, 2024a. URL: <https://arxiv.org/abs/2405.17655>. arXiv:2405.17655.
- P. Suárez, F. Alcántara Ávila, J. Rabault, A. Miró, B. Font, O. Lehmkuhl, R. Vinuesa, Flow control of three-dimensional cylinders transitioning to turbulence via multi-agent reinforcement learning, 2024b. URL: <https://arxiv.org/abs/2405.17210>. arXiv:2405.17210.
- B. Font, F. Alcántara-Ávila, J. Rabault, R. Vinuesa, O. Lehmkuhl, Active flow control of a turbulent separation bubble through deep reinforcement learning, in: *Journal of Physics: Conference Series*, volume 2753, IOP Publishing, 2024, p. 012022.
- R. Vinuesa, O. Lehmkuhl, A. Lozano-Durán, J. Rabault, Flow control in wings and discovery of novel approaches via deep reinforcement learning, *Fluids* 7 (2022) 62.
- L. Prandtl, Über flüssigkeitsbewegung mit kleiner reibung, *Verhandlungen des III. Internationalen Mathematiker-Kongresses*, Heidelberg (1904) 8–13.
- H. Schlichting, K. Gersten, *Boundary-layer theory*, Springer, 2016.
- P. A. Hunter, H. I. Johnson, A flight investigation of the practical problems associated with porous-leading-edge suction, Technical Report, 1954.
- J. J. Cornish, Prevention of turbulent separation by suction through a perforated surface, *Aerophysics Department*, Mississippi State College, 1953.
- A. W. Raspet, Delay of the Stall by Suction Through Distributed Perforation, 587, *Institute of the Aeronautical Sciences*, 1956.
- M. Goodarzi, R. Fereidouni, M. Rahimi, Investigation of flow control over a NACA0012 airfoil by suction effect on aerodynamic characteristics, *Canadian Journal on Mechanical Sciences & Engineering* 3 (2012) 102–109.
- Z. Zhi-yong, Z. Wang-long, C. Zhi-hua, S. Xiao-hui, X. Chen-chao, Suction control of flow separation of a low-aspect-ratio wing at a low Reynolds number, *Fluid Dynamics Research* 50 (2018) 065504.
- C. Chen, R. Seele, I. Wygnanski, Separation and circulation control on an elliptical airfoil by steady blowing, *AIAA journal* 50 (2012) 2235–2247.
- R. Vinuesa, P. Schlatter, Skin-friction control of the flow around a wing section through uniform blowing, in: *Proceedings of European Drag Reduction and Flow Control Meeting (EDRFCM)*, 2017.
- K. Yousefi, R. Saleh, Three-dimensional suction flow control and suction jet length optimization of NACA0012 wing, *Meccanica* 50 (2015) 1481–1494.
- A. Seifert, A. Darabi, I. Wygnanski, Delay of airfoil stall by periodic excitation, *Journal of Aircraft* 33 (1996) 691–698. doi:10.2514/3.47003.
- H. Tang, P. Salunkhe, Y. Zheng, J. Du, Y. Wu, On the use of synthetic jet actuator arrays for active flow separation control, *Experimental Thermal and Fluid Science* 57 (2014) 1–10. doi:10.1016/j.expthermflusci.2014.03.015.
- S. Abdollahipour, Effects of low and high frequency actuation on aerodynamic performance of a supercritical airfoil, *Frontiers in Mechanical Engineering* 9 (2023) 1290074.
- M. Atzori, R. Vinuesa, G. Fahland, A. Stroh, D. Gatti, B. Frohnapef, P. Schlatter, Aerodynamic effects of uniform blowing and suction on a NACA4412 airfoil, *Flow, Turbulence and Combustion* 105 (2020) 735–759. URL: <https://link.springer.com/10.1007/s10494-020-00135-z>. doi:10.1007/s10494-020-00135-z.
- F. Mallor, G. Semprini-Cesari, T. Mukha, S. Rezaeiravesh, P. Schlatter, Bayesian optimization of wall-normal blowing and suction-based flow control of a NACA4412 wing profile, *Flow, Turbulence and Combustion* 113 (2024a) 93–118.
- F. Mallor, R. Vinuesa, R. Örlü, P. Schlatter, High-fidelity simulations of the flow around a NACA4412 wing section at high angles of attack, *International Journal of Heat and Fluid Flow* 110 (2024b) 109590.
- P. F. Fischer, J. W. Lottes, S. G. Kerkemeier, Nek5000 Web page, 2008. <http://nek5000.mcs.anl.gov>.
- A. T. Patera, A spectral element method for fluid dynamics: laminar flow in a channel expansion, *Journal of computa-*

- tional Physics 54 (1984) 468–488.
- Y. Maday, A. T. Patera, Spectral element methods for the incompressible navier-stokes equations, IN: State-of-the-art surveys on computational mechanics (A90-47176 21-64). New York (1989) 71–143.
- P. S. Negi, R. Vinuesa, A. Hanifi, P. Schlatter, D. S. Henningson, Unsteady aerodynamic effects in small-amplitude pitch oscillations of an airfoil, *International Journal of Heat and Fluid Flow* 71 (2018) 378–391.
- G. Eitel-Amor, R. Örlü, P. Schlatter, Simulation and validation of a spatially evolving turbulent boundary layer up to $Re_\theta = 8300$, *International Journal of Heat and Fluid Flow* 47 (2014) 57–69.
- R. Vinuesa, P. S. Negi, M. Atzori, A. Hanifi, D. S. Henningson, P. Schlatter, Turbulent boundary layers around wing sections up to $Re_c = 1,000,000$, *International Journal of Heat and Fluid Flow* 72 (2018) 86–99. doi:[10.1016/j.ijheatfluidflow.2018.04.017](https://doi.org/10.1016/j.ijheatfluidflow.2018.04.017).
- S. M. Hosseini, R. Vinuesa, P. Schlatter, A. Hanifi, D. S. Henningson, Direct numerical simulation of the flow around a wing section at moderate Reynolds number, *International Journal of Heat and Fluid Flow* 61 (2016) 117–128. doi:[10.1016/j.ijheatfluidflow.2016.02.001](https://doi.org/10.1016/j.ijheatfluidflow.2016.02.001), sl TSFP9 special issue.
- D. Massaro, A. Peplinski, R. Stanly, S. Mirzareza, V. Lupi, T. Mukha, P. Schlatter, A comprehensive framework to enhance numerical simulations in the spectral-element code nek5000, *Computer Physics Communications* 302 (2024) 109249.
- R. Vinuesa, P. Schlatter, H. M. Nagib, On minimum aspect ratio for duct flow facilities and the role of side walls in generating secondary flows, *Journal of Turbulence* 16 (2015) 588–606.
- S. Dong, G. E. Karniadakis, C. Chrysosostomidis, A robust and accurate outflow boundary condition for incompressible flow simulations on severely-truncated unbounded domains, *Journal of Computational Physics* 261 (2014) 83–105.
- M. Sato, K. Asada, T. Nonomura, S. Kawai, K. Fujii, Large-eddy simulation of NACA0015 airfoil flow at reynolds number of 1.6×10^6 , *AIAA Journal* 55 (2017) 673–679.
- K. Asada, S. Kawai, Large-eddy simulation of airfoil flow near stall condition at Reynolds number 2.1×10^6 , *Physics of Fluids* 30 (2018).
- Y. Tamaki, S. Kawai, Wall-resolved large-eddy simulation of near-stall airfoil flow at $Re_c = 10^7$, *AIAA Journal* 61 (2023) 698–711.
- F. Mallor, C. S. Vila, M. Hajipour, R. Vinuesa, P. Schlatter, R. Örlü, Experimental characterization of turbulent boundary layers around a NACA4412 wing profile, *Experimental Thermal and Fluid Science* 160 (2025) 111327.
- N. Offermans, Aspects of adaptive mesh refinement in the spectral element method, Ph.D. thesis, KTH Royal Institute of Technology, 2019.
- P. R. Spalart, Comments on the feasibility of les for wings and on the hybrid rans/les approach, in: *Proceedings of the First AFOSR International Conference on DNS/LES*, 1997, 1997, pp. 137–147.
- C. Burstedde, L. C. Wilcox, O. Ghattas, p4est: Scalable algorithms for parallel adaptive mesh refinement on forests of octrees, *SIAM Journal on Scientific Computing* 33 (2011) 1103–1133.
- G. W. Kruse, Parallel nonconforming spectral element solution of the incompressible Navier-Stokes equations in three dimensions, Brown University, 1997.
- C. Mavriplis, A posteriori error estimators for adaptive spectral element techniques, in: *Proceedings of the Eighth GAMM-Conference on Numerical Methods in Fluid Mechanics*, Springer, 1990, pp. 333–342.
- Á. Tanarro, F. Mallor, N. Offermans, A. Peplinski, R. Vinuesa, P. Schlatter, Enabling adaptive mesh refinement for spectral-element simulations of turbulence around wing sections, *Flow, Turbulence and Combustion* 105 (2020) 415–436.
- M. Atzori, R. Vinuesa, A. Stroh, D. Gatti, B. Frohnappfel, P. Schlatter, Uniform blowing and suction applied to nonuniform adverse-pressure-gradient wing boundary layers, *Physical Review Fluids* 6 (2021) 113904. URL: <https://link.aps.org/doi/10.1103/PhysRevFluids.6.113904>. doi:[10.1103/PhysRevFluids.6.113904](https://doi.org/10.1103/PhysRevFluids.6.113904).
- Y. Wang, M. Atzori, R. Vinuesa, Opposition control applied to turbulent wings, *arXiv preprint arXiv:2408.15588* (2024).
- R. Vinuesa, C. Prus, P. Schlatter, H. M. Nagib, Convergence of numerical simulations of turbulent wall-bounded flows and mean cross-flow structure of rectangular ducts, *Meccanica* 51 (2016) 3025–3042.
- P. Poisson-Quinton, Recherches theoriques et experimentales sur le controle de couche limites, in: *Congress of Applied Mechanics*, London, 1948.
- R. Vinuesa, A. Bobke, R. Örlü, P. Schlatter, On determining characteristic length scales in pressure-gradient turbulent boundary layers, *Physics of fluids* 28 (2016).
- Y. Kametani, K. Fukagata, R. Örlü, P. Schlatter, Effect of uniform blowing/suction in a turbulent boundary layer at moderate Reynolds number, *International Journal of Heat and Fluid Flow* 55 (2015) 132–142. URL: <https://linkinghub.elsevier.com/retrieve/pii/S0142727X1500065X>. doi:[10.1016/j.ijheatfluidflow.2015.05.019](https://doi.org/10.1016/j.ijheatfluidflow.2015.05.019).
- R. M. Pinkerton, Calculated and measured pressure distributions over the midspan section of the NACA4412 airfoil, Technical Report, 1937.
- Z. Harun, J. P. Monty, R. Mathis, I. Marusic, Pressure gradient effects on the large-scale structure of turbulent boundary layers, *Journal of Fluid Mechanics* 715 (2013) 477–498.

- R. Pozuelo, Q. Li, P. Schlatter, R. Vinuesa, An adverse-pressure-gradient turbulent boundary layer with nearly constant $\beta \approx 1.4$ up to $Re_\theta \approx 8700$, *Journal of Fluid Mechanics* 939 (2022) A34.
- G. Fahland, M. Atzori, A. Frede, A. Stroh, B. Frohnäpfel, D. Gatti, Drag assessment for boundary layer control schemes with mass injection, *Flow, Turbulence and Combustion* (2023). URL: <https://link.springer.com/10.1007/s10494-023-00462-x>. doi:10.1007/s10494-023-00462-x.
- J. Jeong, F. Hussain, On the identification of a vortex, *Journal of fluid mechanics* 285 (1995) 69–94.
- S. Yarusevych, P. E. Sullivan, J. G. Kawall, On vortex shedding from an airfoil in low-Reynolds-number flows, *Journal of Fluid Mechanics* 632 (2009) 245–271.
- P. Gerontakos, T. Lee, Near wake behind an airfoil with leading-edge flow control., *Journal of aircraft* 42 (2005) 561–568.
- X. Liu, H. Kamliya Jawahar, M. Azarpeyvand, R. Theunissen, Aerodynamic performance and wake development of airfoils with serrated trailing-edges, *AIAA Journal* 55 (2017) 3669–3680.
- S. H. Kim, W. Hong, C. Kim, Separation control mechanism of airfoil using synthetic jet, *Journal of Mechanical Science and Technology* 21 (2007) 1367–1375. doi:10.1007/BF03177422.
- M. Gul, O. Uzol, I. S. Akmandor, An experimental study on active flow control using synthetic jet actuators over S809 airfoil, *Journal of Physics: Conference Series* 524 (2014) 012101. doi:10.1088/1742-6596/524/1/012101.
- C. Çetin, A. Çelik, M. M. Yavuz, Control of flow structure over a nonslender delta wing using periodic blowing, *AIAA Journal* 56 (2018) 90–99. doi:10.2514/1.J056099.
- W. Wu, C. Meneveau, R. Mittal, A. Padovan, C. W. Rowley, L. Cattafesta, Response of a turbulent separation bubble to zero-net-mass-flux jet perturbations, *Physical Review Fluids* 7 (2022) 084601. doi:10.1103/PhysRevFluids.7.084601.
- D. G. Mabey, Analysis and correlation of data on pressure fluctuations in separated flow, *Journal of Aircraft* 9 (1972) 642–645.
- A. Roshko, Controlled unsteady excitation of a reattaching flow, in: *Shear Flow Control Conference*, 1985, p. 552.
- F.-B. Hsiao, C.-F. Liu, J.-Y. Shyu, Control of wall-separated flow by internal acoustic excitation, *AIAA journal* 28 (1990) 1440–1446.
- A. Tuck, J. Soria, Separation control on a naca 0015 airfoil using a 2d micro znmf jet, *Aircraft Engineering and Aerospace Technology* 80 (2008) 175–180.
- A. Carnarius, B. Gunther, F. Thiele, D. Wachsmuth, F. Tröltzsch, J. C. de los Reyes, Numerical study of the optimization of separation control, in: *45th AIAA Aerospace Sciences Meeting and Exhibit*, 2007, p. 58.
- R. Azim, M. Hasan, M. Ali, Numerical investigation on the delay of boundary layer separation by suction for NACA4412, *Procedia Engineering* 105 (2015) 329–334.
- T. Oktay, Ö. Ö. Kanat, Aerodynamic effects of designing a suction channel over NACA4412 wing, *Avrupa Bilim ve Teknoloji Dergisi* (2019) 1001–1007.